Variational pseudo-self-interaction-corrected density functional approach to the *ab initio* description of correlated solids and molecules

A. Filippetti,[1] C. D. Pemmaraju,[2] S. Sanvito,[2] P. Delugas,[1] D. Puggioni,[1] and Vincenzo Fiorentini[1]

[1]*CNR-IOM, UOS Cagliari "SLACS", and Dipartimento di Fisica, Università di Cagliari, I-09042 Monserrato (CA), Italy*

[2]*School of Physics and CRANN, Trinity College, Dublin 2, Ireland*

We present a variational pseudo self-interaction correction density functional approach (VPSIC) to the *ab initio* theoretical description of correlated solids and molecules. The approach generalizes previous nonvariational versions based on plane waves (pseudo self-interaction correction) or atomic orbital (atomic self-interaction correction). The VPSIC approach provides well-defined total energies and forces and enables structural optimization and dynamics, aside from providing high-quality electronic-structure-related properties as the previous methods. A variety of demanding test cases, including nonmagnetic and magnetic correlated oxides (e.g., manganites and d^1 titanates) and a large database of molecules, indicate a high accuracy of the method in predicting structural and electronic properties. This represents a considerable improvement over standard local density functionals at a similar computational cost.

I. INTRODUCTION

The *ab initio*, density functional theory (DFT) based determination of structural and electronic properties of correlated systems remains an outstanding challenge in materials modeling. The crucial bottleneck is that approaches general and powerful enough to tackle the description of strong-correlated systems are also heavily demanding in terms of the required computing resources. This limits the system size that can be practically afforded to at most a few tens of atoms per primitive cell. In contrast, many interesting properties of correlated systems call for large cell sizes already at the bulk level due to the possible coexistence of several competing and juxtaposed orderings (structural, magnetic, orbital, and charge ordering). Furthermore, several much-celebrated phenomenologies such as high-T_c superconductivity in cuprates, colossal magnetoresistivity in manganites, magnetic ordering in diluted magnetic semiconductors, etc., involve doping, the treatment at generic concentration of which is a formidable computing task. Finally, oxide interfaces and multilayers, which are the basis of recent intriguing discoveries such as two-dimensional (2D) electron liquid behavior,[1] may require even a larger simulation effort.

One thus needs to treat routinely a few hundred atoms, a size that can be only afforded at a computational cost similar to that of standard local (spin) density functional theory [L(S)DA] or its generalized gradient approximation (GGA) version. Beyond LSDA, approaches that are agile enough to satisfy this requirement are very few: the very popular LDA + U (Ref. 2) is certainly one of them. A more recent approach with similar characteristics is the pseudo self-interaction correction (PSIC) approach,[3,4] implemented in the past in two different settings: plane-wave basis and ultrasoft pseudopotentials,[3] and localized orbital basis and norm-conserving pseudopotentials [this is called atomic self-interaction correction[5] (ASIC) approach] in the framework of the SIESTA code.[6] LDA + U and PSIC and ASIC move from different conceptual viewpoints: the former introduces an effective Coulomb repulsion, which is typically poorly treated in LSDA. The latter subtracts from the LSDA functional an

approximate (i.e., atomic-orbital-averaged) self-interaction (SI henceforth), that is, the unphysical interaction of an electron with its own generated potential.

Despite this apparent conceptual difference, the two theories act in similar way, i.e., they correct the LSDA eigenvalues by a quantity linearly dependent on orbital occupation. In fact, the PSIC approach may be viewed as a self-consistent all-orbital generalization of the LDA + U correction,[5] but with two distinct advantages over the latter: the ability to cure the LSDA failures in more general situations (i.e., not limited to magnetic and/or orbital-polarized systems) and the absence of an explicit parametric dependence. In PSIC and ASIC approaches, indeed, a role similar to the U correction is played by atomic self-interaction potentials, which are extracted from the free atom (thus, they are universal, i.e., only depend on atomic species) and then incorporated into the band-structure Hamiltonian. At variance with more fundamental SI removal strategies such as the original Perdew-Zunger approach[7] (PZ-SIC), or its later generalization to extended systems,[8,9] which imply dramatic complications in formalism and conceptual interpretation,[4,10] the PSIC approach retains all the simplicity typical of the LDA and GGA: a single-particle potential, which is not explicitly orbital dependent and is translationally invariant (i.e., obeys Bloch symmetry), and an energy functional invariant under unitary rotations of the occupied eigenstates.

The PSIC-ASIC approach demonstrated a consistently improved accuracy in the description of the electronic properties for a vast range of systems[4] at a computational cost not much larger than that of the LSDA itself. The ASIC approach (Ref. 5) is the implementation of choice for large-size systems, as it can easily afford thousands-of-atoms simulations,[11] while the heavier PSIC approach is the standard reference for accuracy. Despite their advantages, the PSIC and ASIC approaches have had limited following so far, for instance, in comparison with the . One reason may be rooted into their lack of variationality. In Ref. 3, the PSIC potential is in fact generated as an ansatz on the single-particle Kohn-Sham (KS) potential, meaning that it does not derive from a germinal

energy functional, a shortcoming precluding access to many ground-state properties, including geometry optimization.

In this paper, we overcome such a limitation by introducing a fully variational version of PSIC and ASIC, named VPSIC. This builds an energy functional that produces, by Euler-Lagrange derivative, a set of single-particle KS equations similar to those of the previous PSIC scheme, thus keeping the successful description of the electronic properties (see Ref. 4 and references therein for a number of case studies), but adding the ability to deliver the ground-state properties expected of standard *ab initio* theories.

Here, we describe these formulations and give ample evidence of the aforementioned capabilities. We present results for both solids (oxides including nonmagnetic aluminates and d^0 titanates, and highly correlated cases such as magnetic d^1 titanates and d^3 manganites) and molecules (a large benchmark molecular database). Extended systems are treated by using the plane-wave-basis implementation and the molecules by using the atomic-orbital basis one. The results presented here indicate that this method is accurate and effective in the study of systems characterized by a wide range of degrees of correlation and localization. Note that other VPSIC results have been already recently presented: a thorough description of the properties of transition-metal monoxides[12] and an account[13] of the properties of 2D electron gas formation at the SrTiO$_3$/LaAlO$_3$ interface.

This paper is organized as follows: In Sec. II, the general formulation is illustrated; in Sec. III, results for nonmagnetic oxide insulators (Sec. III A), titanates (Sec. III B), and manganites (Sec. III C) are presented. Section IV is devoted to illustrate results for molecules. Finally, in Sec. V, we draw our summary and conclusions. Implementation-specific details are discussed in the Appendices: in Appendices A and B, we present an extension of the VPSIC energy functional and forces formulations, respectively, for the case of ultrasoft pseudopotentials (USPP), while Appendices C and D are dedicated to the description of VPSIC energy functional and forces formulation specific for the atomic-orbital basis set.

II. VARIATIONAL PSEUDO-SELF-INTERACTION FORMULATION

In this section, we present the general variational formulation, not related to any specific basis function implementation, of the pseudo-self-interaction approach.

A. VPSIC energy functional and related Kohn-Sham equations

We start from the following VPSIC energy functional:

$$E^{\text{VPSIC}}[\{\psi\}] = E^{\text{LSD}}[\{\psi\}] - \frac{1}{2} \sum_{ij\nu\sigma} \mathcal{E}_{ij\sigma\nu}^{\text{SI}} P_{ji\nu}^{\sigma}, \quad (1)$$

where E^{LSD} is the usual LSDA energy functional

$$E^{\text{LSD}}[\{\psi\}] = T_s[\{\psi\}] + E_{\text{H}}[n] + E_{\text{xc}}[n_+, n_-] + E_{\text{ion}}[\{\psi\}]$$

written as sum of (noninteracting) kinetic (T_s), Hartree (E_{H}), exchange-correlation (E_{xc}), and electron-ion (E_{ion}) energies. Here, ψ are single-particle wave functions, n_+ and n_- are up- and down-polarized electron densities, and $n = n_+ + n_-$. Equation (1) follows the spirit of the original Perdew-Zunger

procedure[7] (hereafter called PZ-SIC) and subtracts from the LSDA total energy a SI term, written as a sum of effective single-particle SI energies ($\mathcal{E}^{\text{SI}}$) rescaled by some orbital occupations P. Here i, j span a set of atomic quantum numbers typically relative to a minimal atomic wave-function basis set [a nondiagonal formulation is necessary to enforce covariancy: $i = (l_i, m_i)$, $j = (l_i, m_j)$ with l and m the angular momentum and the magnetic quantum number, respectively], while σ and ν indicate spin and atomic site, respectively.

The peculiarity of the VPSIC approach resides in the way the second term of Eq. (1) is written for an extended system, the eigenfunctions of which are Bloch states $\psi_{n\mathbf{k}}^{\sigma}$. The orbital occupations are then calculated as the projection of such Bloch states onto localized (e.g., atomic) orbitals, hereafter indicated as $\{\phi\}$:

$$P_{ij\nu}^{\sigma} = \sum_{n\mathbf{k}} f_{n\mathbf{k}}^{\sigma} \langle \psi_{n\mathbf{k}}^{\sigma} | \phi_{i,\nu} \rangle \langle \phi_{j,\nu} | \psi_{n\mathbf{k}}^{\sigma} \rangle, \quad (2)$$

where $f_{n\mathbf{k}}^{\sigma}$ are the Fermi occupancies. For the effective SI energies, we adopt a similar approach, namely,

$$\mathcal{E}_{ij\sigma\nu}^{\text{SI}} = \sum_{n\mathbf{k}} f_{n\mathbf{k}}^{\sigma} \langle \psi_{n\mathbf{k}}^{\sigma} | \gamma_{i,\nu} \rangle C_{ij} \langle \gamma_{j,\nu} | \psi_{n\mathbf{k}}^{\sigma} \rangle, \quad (3)$$

where $\gamma_{i,\nu}$ is the projection function associated to the SI potential of the ith atomic orbital centered on atom ν, and $n_{i\nu}(\mathbf{r}) = \phi_{i\nu}^2(\mathbf{r})$,

$$\gamma_{i\nu}(\mathbf{r} - \mathbf{R}_\nu) = V_{\text{Hxc}}[n_{i\nu}(\mathbf{r} - \mathbf{R}_\nu), 0] \, \phi_{i\nu}(\mathbf{r} - \mathbf{R}_\nu). \quad (4)$$

The Hartree plus exchange-correlation atomic SI potential V_{Hxc} is written in a radial approximation as

$$V_{\text{Hxc}} = V_{\text{H}}[n_{l_i\nu}] + V_{\text{xc}}[n_{l_i\nu}, 0] = \partial E_{\text{Hxc}}[n_{l_i\nu}]/\partial n_{l_i\nu} \quad (5)$$

and calculated at full polarization ($n = n_+$, $n_- = 0$). Finally, C_{ij} are normalization coefficients

$$C_{l_i, m_i, m_j}^{-1} = \int d\mathbf{r} \, \phi_{l_i m_i}(\mathbf{r}) \, V_{\text{Hxc}}[n_{l_i,\nu}(r), 0] \, \phi_{l_i m_j}(\mathbf{r}) \quad (6)$$

with $l_i = l_j$. These are purely atomic and do not depend on the atomic positions. The use of projectors γ in Eq. (3) is aimed at casting the SI energy in fully nonlocal form similar to the fully nonlocal Kleinman-Bylander[14] pseudopotential form, which enables huge savings in computational effort when performing calculations in the reciprocal space.

In order to grasp the idea behind Eqs. (3), (4), and (6), notice that, in the limit of large atomic separation (spin and atomic indexes are dropped for simplicity), the Bloch states $\psi_{n\mathbf{k}}$ and the energies $\mathcal{E}_{ij\sigma\nu}^{\text{SI}}$ become, respectively, the atomic orbitals $\phi_{i\nu}$ and the atomic SI energies

$$\epsilon_i^{\text{SI}} = \int d\mathbf{r} \, n_i(\mathbf{r}) \, \{V_{\text{H}}[n_i(\mathbf{r})] + V_{\text{xc}}[n_i(\mathbf{r}), 0]\}. \quad (7)$$

Thus, the orbital occupations $P_{ij\nu}^{\sigma}$ (if suitably normalized) act as scaling factors for the atomic SI energies, which are then assumed to be the upper limit of the SI correction amplitude. We remark that, in the atomic limit, Eq. (1) recovers the PZ-SIC total energy expression only for the Hartree SI part. Our SI *exchange-correlation* energy density, instead, is

$$\frac{1}{2} V_{\text{xc}}[n_i, 0] = \frac{1}{2} \left[\epsilon_{\text{xc}} + n_i \frac{\partial \epsilon_{\text{xc}}}{\partial n_i} \right], \quad (8)$$

which differs from the PZ-SIC expression $\epsilon_{xc}[n_i, 0]$.

From Eq. (1), we obtain the corresponding VPSIC KS equations through the usual Euler-Lagrange derivative

$$\frac{\partial E^{\text{VPSIC}}}{\partial \psi_{n\mathbf{k}\sigma}^*} = \tilde{\epsilon}_{n\mathbf{k}\sigma} \, \psi_{n\mathbf{k}\sigma} = \hat{h}_\sigma^{\text{LSD}} \psi_{n\mathbf{k}\sigma}$$
$$-\frac{1}{2} \sum_{ij\nu} \left\{ \frac{\partial \mathcal{E}_{ij\sigma\nu}^{\text{SI}}}{\partial \psi_{n\mathbf{k}\sigma}^*} P_{ji\nu}^\sigma + \mathcal{E}_{ij\sigma\nu}^{\text{SI}} \frac{\partial P_{ji\nu}^\sigma}{\partial \psi_{n\mathbf{k}\sigma}^*} \right\}, \quad (9)$$

where $\tilde{\epsilon}_{n\mathbf{k}\sigma}$ are VPSIC eigenvalues and

$$h_\sigma^{\text{LSD}}(\mathbf{r}) = -\frac{\nabla_{\mathbf{r}}^2}{2} + V_{\text{H}}[n(\mathbf{r})]$$
$$+ V_{xc}[n_+(\mathbf{r}), n_-(\mathbf{r})] + V_{\text{ion}}(\mathbf{r}) \quad (10)$$

is the usual KS LSDA Hamiltonian and

$$\frac{\partial \mathcal{E}_{ij\sigma\nu}^{\text{SI}}}{\partial \psi_{n\mathbf{k}\sigma}^*} = |\gamma_{i,\nu}\rangle C_{ij\nu} \langle \gamma_{j,\nu} | \psi_{n\mathbf{k}}^\sigma \rangle, \quad (11)$$

$$\frac{\partial P_{ji\nu}^\sigma}{\partial \psi_{n\mathbf{k}\sigma}^*} = |\phi_{j,\nu}\rangle \langle \phi_{i,\nu} | \psi_{n\mathbf{k}}^\sigma \rangle. \quad (12)$$

The first sum term in curly brackets in Eq. (9) corresponds to the SI potential projector written as in the original PSIC KS equations.[3] Since the two sums in the curly brackets essentially describe the same physical quantity (i.e., the SI potential), in practice, they give similar results when applied to a Bloch state. It follows that Eq. (9) describes an energy spectrum substantially similar to that of our previous nonvariational scheme, but with the advantage to derive from the VPSIC energy functional via the Euler-Lagrange construction.

In DFT, it is customary to rewrite the total energy in terms of the sum of the Kohn-Sham eigenvalues. By writing $\epsilon_{nk\sigma}$ as the LSDA eigenvalues, it is easy to verify that

$$\sum_{n\mathbf{k}\sigma} f_{n\mathbf{k}}^\sigma \tilde{\epsilon}_{nk\sigma} = \sum_{n\mathbf{k}\sigma} f_{n\mathbf{k}}^\sigma \left\langle \psi_{n\mathbf{k}}^\sigma \left| \frac{\partial E^{\text{VPSIC}}}{\partial \psi_{n\mathbf{k}\sigma}^*} \right. \right\rangle$$
$$= \sum_{n\mathbf{k}\sigma} f_{n\mathbf{k}}^\sigma \epsilon_{nk\sigma} - \sum_{ij\sigma\nu} \mathcal{E}_{ij\sigma\nu}^{\text{SI}} P_{ji\nu}^\sigma. \quad (13)$$

Equation (1) can then be rewritten as

$$E^{\text{VPSIC}}[\{\psi\}] = \tilde{E}^{\text{LSD}}[\{\psi\}] + \frac{1}{2} \sum_{ij\sigma\nu} \mathcal{E}_{ij\sigma\nu}^{\text{SI}} P_{ji\nu}^\sigma, \quad (14)$$

where

$$\tilde{E}^{\text{LSD}}[\{\psi\}] = \sum_{n\mathbf{k}\sigma} f_{n\mathbf{k}}^\sigma \tilde{\epsilon}_{nk\sigma} + E_{\text{Hxc}}[n_+(\mathbf{r}), n_-(\mathbf{r})]$$
$$+ E_{\text{ion}} - \sum_\sigma \int d\mathbf{r} \, n_\sigma(\mathbf{r}) V_{\text{Hxc}}^\sigma[n_+(\mathbf{r}), n_-(\mathbf{r})] \quad (15)$$

is the LSDA energy functional where the VPSIC eigenvalues now replace those of the LSDA.

Finally, in the original PSIC formulation, the SI V_{Hxc} potential is rescaled by a relaxation factor $\alpha = 1/2$ to take into account the screening (i.e., the suppression) of atomic self-interaction by the surrounding charge of the extended system (see Ref. 4 for an extended discussion). Careful tests on a large set of solids[5] show that this value is adequate for a

vast array of crystalline systems, whereas for molecules, a full atomic SI ($\alpha = 1$) is more appropriate. We keep this empirical recipe also in our present formulation.

B. Simplified variants of VPSIC approach and relation with the original nonvariational method

From the general expression of Eq. (1), two interesting subcases can be derived. By assuming fixed (i.e., non- self-consistently calculated) orbital occupations P_{ij} in Eq. (9), the second term in the curly brackets vanishes and the VPSIC KS equations reduce to those of the original PSIC scheme of Ref. 3. Indeed, it was previously pointed out[4] that the original scheme becomes variational at fixed orbital occupations.

Another useful subcase is obtained by replacing Eq. (3) with the simplified expression

$$\mathcal{E}_{ij\sigma\nu}^{\text{SI}} = P_{ij\nu}^\sigma \epsilon_{i\nu}^{\text{SI}} = P_{l_i m_i m_j\nu}^\sigma \epsilon_{l_i\nu}^{\text{SI}}, \quad (16)$$

where the atomic $\epsilon_{l_i\nu}^{\text{SI}}$ (in radial approximation) is given by Eq. (7). By using Eq. (15), Eqs. (1) and (9) become, respectively,

$$E^{\text{VPSIC}_0}[\{\psi\}] = E^{\text{LSD}}[\{\psi\}] - \frac{1}{2} \sum_{ij\nu\sigma} P_{ij\nu}^\sigma P_{ji\nu}^\sigma \epsilon_{j\nu}^{\text{SI}}$$
$$= \tilde{E}^{\text{LSD}}[\{\psi\}] + \frac{1}{2} \sum_{ij\nu\sigma} P_{ij\nu}^\sigma P_{ji\nu}^\sigma \epsilon_{j\nu}^{\text{SI}} \quad (17)$$

and

$$\frac{\partial E^{\text{VPSIC}_0}}{\partial \psi_{n\mathbf{k}\sigma}^*} = \hat{h}_\sigma^{\text{LSD}} \psi_{n\mathbf{k}\sigma} - \sum_{ij\nu} P_{ij\nu}^\sigma \frac{\partial P_{ji\nu}^\sigma}{\partial \psi_{n\mathbf{k}\sigma}^*} \epsilon_{j\nu}^{\text{SI}}. \quad (18)$$

This simplified VPSIC formalism (hereafter indicated as VPSIC$_0$) is a computationally convenient alternative (especially in terms of memory) to perform structural optimizations in large-size systems. In Sec. III, we will show that, for nonmagnetic semiconductors and insulators, it provides electronic and structural properties in good agreement with those calculated with the complete VPSIC approach. However, VPSIC$_0$ is typically less satisfactory for the electronic properties of magnetic materials.

C. Forces formulation

In the VPSIC approach, the atomic forces formulation follows from the usual Hellmann-Feynman procedure. It is obtained as the LSDA expression augmented by a further additive contribution due to the atomic-site dependence of the SI projectors

$$-\frac{\partial E^{\text{VPSIC}}[\{\psi\}]}{\partial \mathbf{R}_\nu} = \mathbf{F}_\nu^{\text{LSD}}$$
$$+ \frac{1}{2} \sum_{ij,n\mathbf{k}\sigma} f_{n\mathbf{k}}^\sigma \left\{ \left\langle \psi_{n\mathbf{k}}^\sigma \left| \frac{\partial \gamma_{i,\nu}}{\partial \mathbf{R}_\nu} \right\rangle C_{ij} \langle \gamma_{j,\nu} | \psi_{n\mathbf{k}}^\sigma \rangle P_{ji\nu}^\sigma[\{\psi\}] \right. \right\}$$
$$+ \frac{1}{2} \sum_{ij,n\mathbf{k}\sigma} f_{n\mathbf{k}}^\sigma \left\{ \mathcal{E}_{ij\sigma\nu}^{\text{SI}}[\{\psi\}] \left\langle \psi_{n\mathbf{k}}^\sigma \left| \frac{\partial \phi_{i,\nu}}{\partial \mathbf{R}_\nu} \right\rangle \langle \phi_{j,\nu} | \psi_{n\mathbf{k}}^\sigma \rangle \right. \right\}. \quad (19)$$

The complex conjugate must be summed to the terms in curly brackets.

In the simplified $VPSIC_0$ version, the term to be added to $\mathbf{F}_\nu^{\mathrm{LSD}}$ reduces to

$$\sum_{ij,nk\sigma} f_{n\mathbf{k}}^\sigma \left\{ P_{ij\nu}^\sigma \epsilon_{j\nu}^{\mathrm{SI}} \left\langle \psi_{n\mathbf{k}}^\sigma \left| \frac{\partial \phi_{j,\nu}}{\partial \mathbf{R}_\nu} \right\rangle \langle \phi_{i,\nu} | \psi_{n\mathbf{k}}^\sigma \rangle \right\} \qquad (20)$$

with complex conjugate sum also implied.

In writing Eqs. (19) and (20), we have assumed that the force acting on a given atom ν only depends on the single atomic projector centered on ν itself. Such an assumption is not necessarily true if the orbital occupations are to be reorthonormalized in the cell. This choice, which complicates significantly the formulation described above, is discussed in detail in the Appendices together with the specific implementations to the plane waves plus USPP and the local orbital plus norm-conserving pseudopotential approaches.

III. RESULTS: EXTENDED SYSTEMS

As pointed out in the previous sections, there is a substantial formal similarity between the KS equations derived for VPSIC and PSIC and ASIC. As this section proves, the long series of results for the electronic properties of many solids obtained with PSIC and ASIC approaches in recent years are confirmed by the theoretical framework presented here. Namely, the VPSIC approach gives only marginal differences with respect to PSIC and ASIC as the band energies and the densities of states (DOSs) are concerned. Hereafter, we consider as test cases for VPSIC a number of materials, either never tackled before (d^1 titanates) or revisited (e.g., $CaMnO_3$), to specifically address total energy-derived properties such as the equilibrium structure and the magnetic exchange interactions.

Specifically, we have selected three classes of solids, which, at the same time, test the broad spectrum of applicability of the VPSIC approach and are interesting compounds by themselves, both from the conceptual and the technological points of view. These are wide-gap oxide insulators, magnetic titanates representative of the $3d$-t_{2g} Mott-insulating perovskites and magnetic manganites representative of the $3d$-e_g charge-transfer insulating perovskites.

Calculations are carried out with ultrasoft pseudopotentials[15] and a plane-wave basis set with cutoff energy ranging from 30 to 35 Ryd depending on the specific system, $6 \times 6 \times 6$ special k-point grids for self-consistent calculations, $10 \times 10 \times 10$ special k points, and linear tetrahedron interpolation method for the DOS. The Ceperley-Alder-Perdew-Zunger[7] local density approximation is used for the exchange-correlation functional. Structural relaxations are carried out with a threshold of 1 mRy/Bohr $\sim$0.02 eV/Å on the largest force component.

A. Wide-gap insulators: $LaAlO_3$, $SrTiO_3$, and TiO_2

As prototypes of nonmagnetic wide-gap insulators, we selected materials widely in use in the field of functional oxides, rutile TiO_2, and the perovskite $LaAlO_3$ and $SrTiO_3$. Given the abundant theoretical and experimental results already available, these represent ideal test cases for the VPSIC approach.

For nonmagnetic oxides, the level of accuracy of standard LDA calculations may vary according to the property
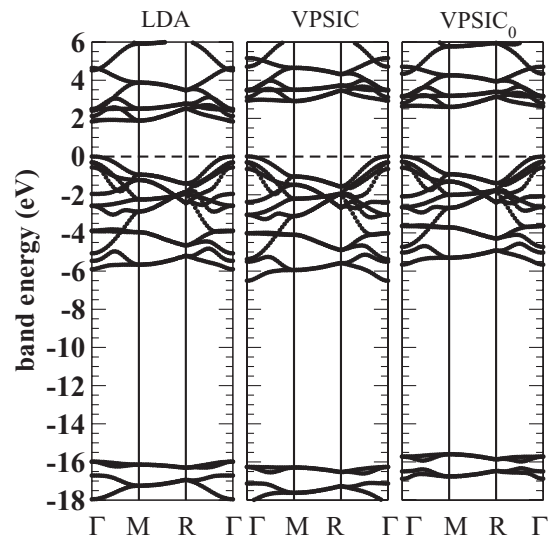

FIG. 1. Band energies of TiO_2 (rutile) calculated at experimental lattice structure ($a = 4.59$ Å, $c/a = 0.664$, $u = 0.305$) calculated by LDA, VPSIC, and $VPSIC_0$. The k-point coordinates (units of $\pi/a = \pi/b$, π/c) are $\Gamma = (0,0,0)$, $M = (1,1,0)$, $R = (1,1,1)$.

investigated. Typically, a good rendition of structural properties is juxtaposed to an unsatisfactory match of the calculated band-structure and interband transition energies, involving the well-known underestimation of the fundamental band gap and the poor description of transition-metal d and (to a lesser extent) oxygen p states. We find that the VPSIC approach systematically improves the electronic properties over the LSDA, while preserving a similar accuracy for structural properties. In any comparison, it must be kept in mind that subtleties in the results may (and usually do) vary appreciably depending on a number of computational details largely independent of the underlying formalism (e.g., the type of wave-function basis set, the type of pseudopotentials, etc.) and yet typical of this class of simulations. In order to achieve an evaluation as unbiased as possible, it is useful to compare the VPSIC results with experiments as well as with their LDA counterparts, obtained for identical computational details.

We start our analysis by looking at the electronic structure. The band structures calculated within VPSIC, $VPSIC_0$, and LDA are displayed in Figs. 1, 2, and 3 for TiO_2, $SrTiO_3$, and $LaAlO_3$, respectively. The corresponding gap values are reported in Table I. For an unbiased comparison, the bands are calculated at the same (experimental) structure.

As expected, the TiO_2 (Fig. 1) gap opens between occupied O $2p$ valence and empty Ti $3d$ conduction bands. According to the VPSIC, the minimum gap is indirect between Γ at valence-band top (VBT) and M (i.e., the BZ edge along [110]) at the conduction-band bottom (CBB), while the direct gap is at Γ. The gap values are in satisfactory good agreement with the experiments, while the LDA results present the well-known band-gap underestimation of nearly 40%, a typical LDA error bar for nonmagnetic insulators. In contrast, the $VPSIC_0$ operates a partial (about 80%) recovery of the correct energy gap over the LDA result. While this may be unsatisfactory for the prediction of the optical spectra, it is sufficient for structural optimization at a pace substantially similar to that
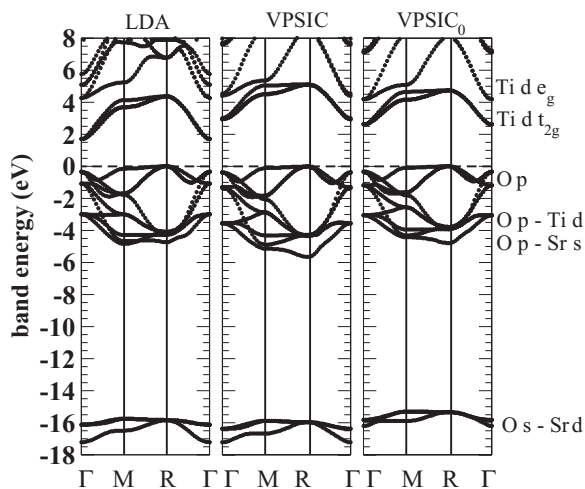
FIG. 2. Band energies of cubic $SrTiO_3$ calculated at experimental lattice structure ($a = 3.92$ Å). The k-point coordinates (units of π/a) are $\Gamma = (0,0,0)$, $M = (1,1,0)$, $R = (1,1,1)$.

of LDA itself. Notice that VPSIC and $VPSIC_0$ change the (mainly O $2p$) valence bandwidth (~6.5 eV for VPSIC, 5.7 eV for $VPSIC_0$) in opposite directions from the LDA value (~6.0 eV); this illustrates the fact that the $VPSIC_0$ is not simply a rescaled VPSIC.

It is worth emphasizing that the VPSIC (or $VPSIC_0$) ability to correct the LDA gap problem in nonmagnetic oxides, the ground state of which is only residually affected by d-type orbitals, spurs from its all-orbital corrective character (in particular, from corrections to the O $2p$ band). In contrast, the GGA + U band gap of 2.2 eV (with $U = 3.4$ eV applied to Ti $3d$) calculated in Ref. 21, is only marginally larger than the GGA value of 1.9 eV. The necessity of applying a corrective U onto the O $2p$ orbital energies was indeed discussed in previous works.[22]

We now turn to $SrTiO_3$, for which we adopt the cubic structure to avoid structural bias. The band structure is reported in Fig. 2. The dominant (and, where relevant, the secondary) orbital character for each group of bands is also reported in
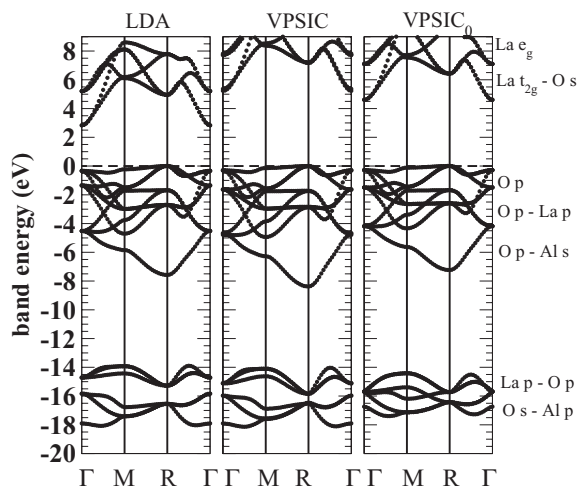

FIG. 3. Band energies of cubic $LaAlO_3$ calculated at experimental lattice structure ($a = 3.82$ Å). The k points are the same as in Fig. 2.

TABLE I. Direct (ΔE_d) and indirect (ΔE_i) band-gap energies and O $2p$ manifold valence bandwidth (W_{Op}) in eV, calculated within LDA, VPSIC, and $VPSIC_0$, compared to the experimental values.

		LDA	VPSIC	$VPSIC_0$	Expt.
TiO_2	ΔE_i (Γ-L)	1.88	2.90	2.59	
	ΔE_d (Γ)	1.84	2.93	2.62	[3.0,3.1] (Refs. 16,17)
	W_{Op}	6.0	6.5	5.7	~7 (Ref. 18)
$SrTiO_3$	ΔE_i (M-Γ)	1.69	2.94	2.62	3.25 (Ref. 19)
	ΔE_d (Γ)	2.04	3.30	2.95	3.75 (Ref. 19)
	W_{Op}	5.0	5.5	4.8	~6 (Ref. 20)
$LaAlO_3$	ΔE_i (M-Γ)	2.83	5.23	4.61	
	ΔE_d (Γ)	3.17	5.51	4.89	5.6
	W_{Op}	7.6	8.38	7.27	~8–9 (Ref. 20)

the figure. The energy gap opens between a VBT dominated by the O $2p$ orbitals and a CBB of mainly Ti $3d$ character, with the Sr $4d$ contributions placed at higher energies. We can see in Table I that the LDA band gaps are only $\sim55\%$ of the experimental direct (3.25 eV) and indirect (3.75 eV) gaps. The VPSIC approach, in contrast, recovers most ($\sim90\%$), although not all, of the LDA discrepancy. This is, in part, attributed rather than to a VPSIC insufficiency to a much too small LDA value originating from the specific LDA flavor and the pseudopotentials used. Indeed, previous LDA determinations[19,23] gave 1.9 and 2.24 eV, respectively, for the indirect and direct band gaps, and a "scissor" operator of 1.5 eV was employed in Ref. 19 to readjust the band energies to match ellipsometry data. According to our calculations, the VPSIC approach provides a "scissor" shift of about 1.3 eV with respect to the LDA. While in general the action of the VPSIC approach over the LDA bands can be remarkably k-point dependent, for these wide-gap, highly ionic, nonmagnetic oxides, the LDA band dispersion is not modified significantly. This fact provides an *a posteriori* justification of the use of a scissor operator.

However, while the band shape is little altered, the bandwidths change appreciably. Consider, for example, the first unoccupied doublet of Ti $3d$ t_{2g} character: in LDA, this spans about 2.5 eV, while in VPSIC or $VPSIC_0$, it is reduced to about 2 eV. This is a consequence of the enhanced localization (i.e., reduced p-d hybridization), which typically follows from the removal of SI. In contrast, the VPSIC approach increases the LDA O $2p$ bandwidth because of its different spectral weight distribution, namely, the top manifold is purely O $2p$, while the bottom (R point) shows a significant admixture of Ti $3d$ and Sr $3s$ states. The different effective SI energies related to these different orbital characters eventually stretches the band bottom down to lower energies, thus resulting in an increase of bandwidth. In $VPSIC_0$, the effective SI energies are fixed to their atomic counterparts, thus, that the effect over the LDA values is more that of a rigid band shift.

Finally, we turn our attention to cubic $LaAlO_3$, the calculated band structure of which is presented in Fig. 3. The energy gap is between the O $2p$ valence bands and the conduction band of mainly Al s-p character. The absence of $3d$ states produces an observed gap (5.6 eV) much larger than that in $SrTiO_3$, but still grossly underestimated by the LDA ($\sim56\%$ of the experimental value). This prototypical case demonstrates the need to repair the LDA irrespective of the presence or the
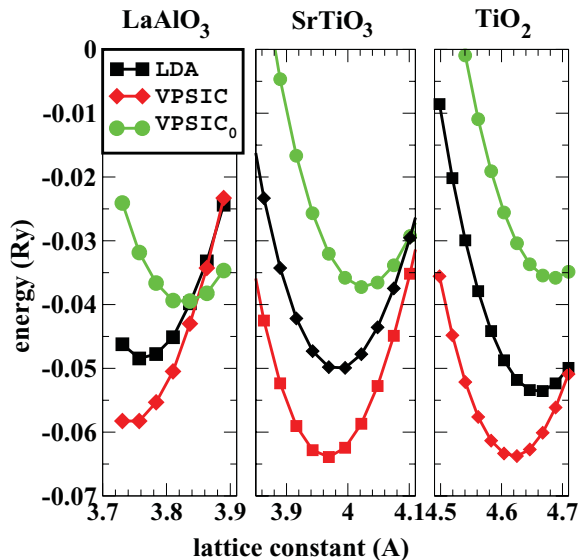
FIG. 4. (Color online) Total energies as a function of lattice parameter for cubic $SrTiO_3$, $LaAlO_3$, and tetragonal TiO_2 as calculated by LDA, VPSIC, and $VPSIC_0$.

absence of $3d$ states. Again, both VPSIC and $VPSIC_0$ recover a satisfying energy gap. However, as in the case of $SrTiO_3$, they act differently on the bandwidths: VPSIC stretches the bottom of valence O $2p$ manifold down to lower energies, while for $VPSIC_0$, the same bands now span an energy window even smaller than that of the LDA. The low-lying O s bands (between -16 and -18 eV) and La p semicore bands (at around -14 eV) are described similarly by LDA and VPSIC. Notably, $VPSIC_0$ finds instead almost no separation between the two groups.

Having compared the band structures for fixed crystal structures, we now consider structural parameters. In Fig. 4, we report total energies versus lattice parameter for cubic $SrTiO_3$, $LaAlO_3$, and rutile TiO_2 calculated within LDA, VPSIC, and $VPSIC_0$. The calculated equilibrium parameters are compared in Table II with the available experimental values. We start the analysis by considering the reference LDA values. As mentioned previously, the LDA is typically satisfactory for what concerns the structural properties, but the level of accuracy may vary depending on the technicalities of the calculation. While LDA generally underestimates the equilibrium lattice constants by about 1%, for $SrTiO_3$ and TiO_2, we find overestimates as large as $\sim 1.5\%$ when

TABLE II. Lattice parameters (in Å) calculated within LDA, VPSIC, and $VPSIC_0$ compared to the experimental values. For $SrTiO_3$ and $LaAlO_3$, the cubic symmetry is assumed, while TiO_2 is in its tetragonal (rutile) structure. For TiO_2, c/a is fixed to the experimental value 0.644, while the internal parameter u is calculated.

	LDA	PSIC	$PSIC_0$	Expt.
$SrTiO_3$	3.99	3.97	4.02	3.92
$LaAlO_3$	3.76	3.74	3.83	3.82
TiO_2 a	4.67	4.62	4.69	4.59
TiO_2 u	0.3021	0.3066	0.3066	0.3048

compared to experiments. In contrast, the lattice constant of $LaAlO_3$ is underestimated by little more than 1%. The VPSIC approach operates a systematic (0.5%–1%) reduction of the corresponding LDA values and ends up to be in very good agreement with the experiments (within 1%) for $SrTiO_3$ and TiO_2, and to a slightly less satisfactory agreement (-2%) for $LaAlO_3$. $VPSIC_0$ again corrects in the opposite direction and it systematically increases the LDA values by 0.5%–1%.

The different behavior of VPSIC and $VPSIC_0$ can be easily linked back to our previous findings about the band structure. In fact, VPSIC widens the occupied valence-band manifold (O $2p$, O $2s$) with respect to the LDA, it reduces the effective screening and, thus, the bond length gets reduced. In contrast, the $VPSIC_0$ shrinks the occupied band manifolds with respect to the LDA, and it causes an increase of effective screening and, thus, of the bond length. The shrinking of equilibrium volume caused by the VPSIC approach was also reported for transition-metal monoxides MnO and NiO.[12] Clearly, this should not be intended as a universal trend, as the bandwidth and the charge localization are material-dependent quantities, and such are the VPSIC modifications over the LDA electronic structure.

We conclude this section by emphasizing the overall good quality of the VPSIC predictions for the three compounds examined. These present lattice parameters and energy band gaps are, respectively, 1%–2% and $\sim 10\%$ within the experimental values. While additional studies will be necessary for a full assessment of the theory, the results of this section should definitely encourage the use of the VPSIC approach for the investigation of wide-gap oxide insulators.

B. Magnetic d^1 titanates: $YTiO_3$, $LaTiO_3$

Magnetic titanates $LaTiO_3$ and $YTiO_3$ are the subject of a long-standing and still ongoing debate. Titanates, characterized by the nominal Ti d^1 configuration, rank among the most peculiar and intriguing magnetic perovskites. At variance with manganites and cuprates, the fundamental chemistry of which is governed by the $3d$ e_g states, in titanates, the $3d$ valence states have t_{2g} symmetry, thus, they are orbitals not directly oriented toward the oxygens. This produces a much weaker p-d hybridization and a crystal field splitting smaller than in e_g systems. Indeed, experiments show that the phenomenology of these materials is crucially affected by small structural details.

A nice illustration of the highly sensitive magnetostructural coupling is provided by the comparative study of $YTiO_3$ (YTO) and $LaTiO_3$ (LTO). Both materials are *Pnma* perovskites, with relatively small Jahn-Teller distortions and large $GdFeO_3$-type rotations of the Ti-centered octahedra. In agreement with the classic space-filling criterion, the difference in the A-cation size (with La being bigger than Y) enhances both distortions and rotations in YTO compared to LTO. These relatively subtle differences, in turn, lead to quite different magnetic behaviors. YTO is ferromagnetic[24–26] (FM) with a Curie temperature $T_C = 30$ K, a sizable band gap (~ 1 eV), and a magnetic moment of 0.8 μ_B per formula unit, in agreement with a Ti d^1 ionic configuration. In contrast, LTO is G-type antiferromagnetic[27] (AF) with a Néel temperature $T_N = 130$ K, a very small energy gap (~ 0.05–0.2 eV), and considerably smaller magnetic moment (~ 0.57 μ_B).[28]

Attempts to explain the small magnetic moment and the nearly isotropic spin-wave dispersion[29] in LaTiO$_3$ have generated substantial debate. It was pointed out that a single electron in the triple-degenerate t_{2g} manifold may quantum fluctuate, giving rise to an exotic orbital-liquid state.[30,31] However this fascinating hypothesis is contrasted by a body of evidences[27,28,30,32–35] showing that the crystal field splitting is actually not small enough to maintain the t_{2g} degeneracy substantially unlifted. As a consequence, a Jahn-Teller distorted orbital-ordered state is realized in LTO as well as in YTO.

It is needless to say that these issues have stimulated a number of attempts at describing the titanates with *ab initio* approaches, including LSDA,[36] LDA + U,[37,38] and several LSDA + DMFT calculations.[39–41] The VPSIC results presented here are a valuable addition to this rich literature since they give an internally coherent description of the structural and electronic properties on a purely *ab initio* basis, in the framework of the same theory and without system-dependent parameters (e.g., U, J). Here we proceed by first illustrating the electronic properties of YTO calculated at the experimental lattice structure as a prototypical t_{2g} system. We then move on to the more peculiar LTO and highlight the differences with respect to YTO. Then, we conclude with the structural properties of both systems, which rationalize their different behavior. We note in passing that LSDA predicts a nonmagnetic metallic electronic ground state and can not, therefore, be meaningfully compared with the VPSIC approach in this case.

Figure 5 shows the orbital-resolved DOS of YTO. The occupied DOS has two major contributions: at the VBT, there is a ~0.8-eV-wide fully spin-polarized peak associated to the Ti 3d states (and some residual hybridization with a small O 2p fraction). Although the nominal configuration is Ti^{3+} d^1, a small amount of Ti d-O p hybridization is clearly visible (notice the scale, though: here, the O 2p weight is way smaller than, e.g., that in manganites). It follows that the calculated static charges and magnetic moment differ considerably from their nominal values. For Ti, we obtain ~1.6 and ~0.7 electrons for up- and down-polarized 3d state, respectively, with a magnetic moment of 0.92 μ_B, slightly larger than the experimentally observed 0.8 μ_B. At much lower energies (–4 to –8 eV below the Ti 3d peak), there is a broader, unpolarized DOS of O 2p character, not shown in the figure. The CBB bands are also dominated by Ti 3d t_{2g} states, residually hybridized with O 2p and Y 4d. Thus, YTO falls unambiguously in the category of true Mott-Hubbard insulators, at variance with most manganites or cuprates, which are actually charge-transfer insulators or in an intermediate regime (we will come back to this important point later on).

In the band energy plot for FM YTO (see Fig. 6, left panel), we observe four occupied bands (one for each Ti) separated from the 3d empty conduction bands by 1.8 eV. The fundamental gap only involves majority bands and it is direct at Γ. The CBB bands span a ~1-eV-wide interval. According to our calculations, the sharp DOS peak at the valence top is a complex admixture of the five Ti 3d orbitals.

In order to analyze quantitatively the identity of this state, we diagonalize the corresponding $P_{mm'}^\sigma$ density matrix in the 3d orbital subspace. The results are reported in Table III for two coordinate systems: the orthorhombic $\sqrt{2} \times \sqrt{2} \times 2$ *Pnma* (x', y', z') and the conventional cubic (x, y, z), which differ by
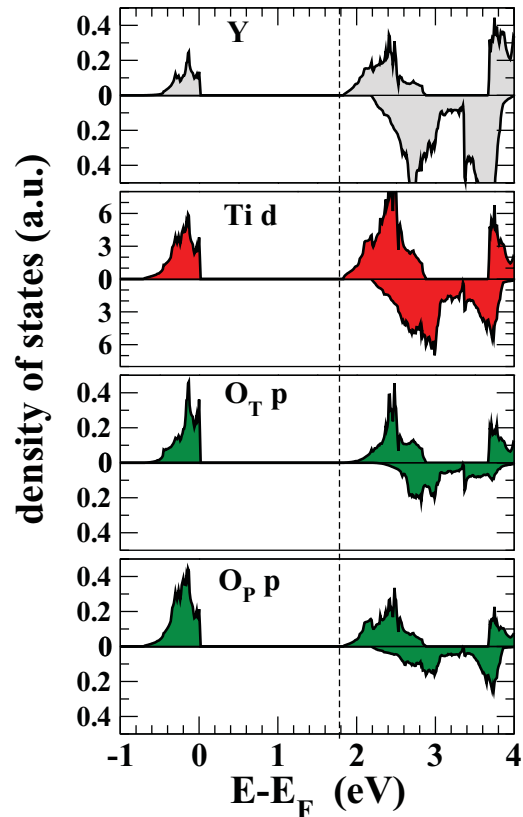

FIG. 5. (Color online) Orbital-resolved DOS for FM YTO. For clarity, only Ti 3d, Y 5d, and O 2p are shown (O on top and in the Ti plane are labeled O$_T$ and O$_P$, respectively). Note that the Y and O DOS scale has been magnified for clarity. For each of the panels, the upper half corresponds to majority spins and the lower one to the minority.

a 45° rotation[42] of the (x, y) plane. Let us focus first our attention on the Ti ion placed at $(0,0,0)$ in the cubic YTO reference system. This shows prevailing contributions from the $|yz\rangle$ and $|xy\rangle$ orbitals. However, also the e_g contributions are not completely negligible. The corresponding state can be expressed as $|\Psi_1\rangle \sim 0.75|yz\rangle + 0.56|xy\rangle$, as visually confirmed by the charge density isosurface plot in the left panel of Fig. 7. The same figure highlights the resulting orbital ordering: coplanar states show an alternance of dominant $|yz\rangle$ and $|xz\rangle$ contributions, plus a change in sign for $|xy\rangle$, which causes the lobes of $|yz\rangle$ (or $|xz\rangle$) to lean back and forth toward the (x, y) plane (i.e., $|\Psi_2\rangle \sim 0.75|xz\rangle - 0.56|xy\rangle$). In contrast, states aligned along z only differ by the alternance of $|xy\rangle$ sign, thus, $|\Psi_3\rangle \sim 0.75|yz\rangle - 0.56|xy\rangle$ and $|\Psi_4\rangle \sim 0.75 |xz\rangle + 0.56|xy\rangle$. Our results are in excellent agreement with linear-dichroism x-ray absorption,[43] which gives 0.8 and 0.6 for the coefficients of the two most occupied t_{2g} orbitals,[44] and with the LDA + DMFT results[39] giving 0.78 and 0.62, respectively.

Now, we move to analyze the results for LTO. Remarkable differences from YTO emerge from the calculated DOS (Fig. 8) and band structure (Fig. 6): the fundamental band gap is slightly smaller for LTO, but still quite sizable (1.6 eV); furthermore, the bands are flatter than in YTO (the occupied 3d states at VBT are only 0.4 eV wide) and the hybridization
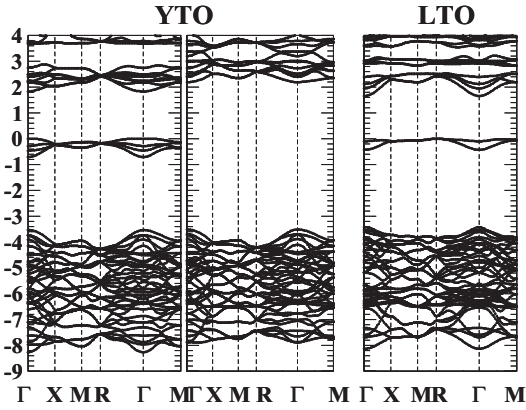
FIG. 6. Band structure of FM YTO (left, up spin; right, down spin) and AF-G LTO (right).

with O is even more marginal, although still visible. Even the conduction bands in LTO appear flatter and, in fact, they are separated in two groups by a gap of 0.2 eV. The magnetic moment is 0.89 μ_B, similar to that of YTO.

The difference with YTO is also clearly borne out by the diagonalized density matrix reported in Table III. By looking at the cubic reference system, one can see that the e_g contribution is now almost vanishing (at variance with YTO) and the occupied states have essentially a pure t_{2g} character. Moreover, the diversification of the t_{2g} occupancies is much reduced with respect to YTO as a result of the smaller rotations. This state approximately shapes as cigar-shaped [111]-directed lobes resulting from the nearly even t_{2g} combination, as the corresponding charge density isosurface plot of Fig. 7 (right
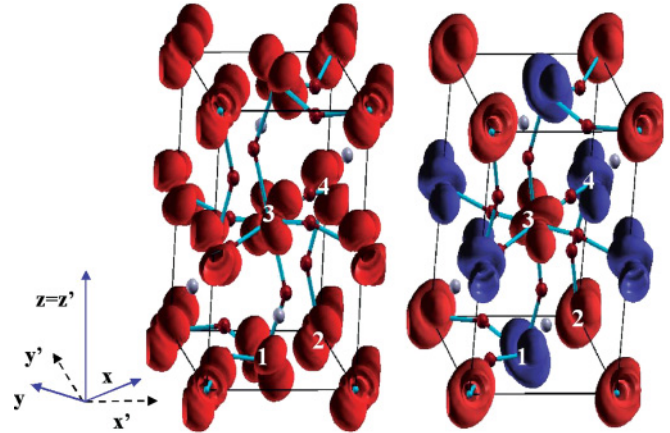

FIG. 7. (Color online) Charge density isosurface $n_\pm = \pm 0.01$ electrons/cm^3 of the upmost occupied state for FM YTO (left) and AF-G LTO (right). Red (light) and blue (dark) surfaces represent spin majority (+) and minority (−) contributions, respectively. On this scale, only Ti d contributions are visible (oxygen contributes residually; see the DOS in Figs. 5 and 8). Both YTO and LTO are orbital ordered, i.e., the four Ti atoms in the cell have the same integrated charge, but different orbital distribution. The numbers label each Ti relative to the orbital decomposition in Table III.

panel) confirms. Note that, if the t_{2g} coefficients were exactly the same, Ψ_1 and Ψ_2 as well as Ψ_3 and Ψ_4 would have been identical and the resulting "cigars" in each plane would have been exactly parallel to each other and pointing along [111].

Although the orbital charge distribution in YTO and LTO is markedly different and causes much of their macroscopic differences, the relative ordering is the same. In fact, also for
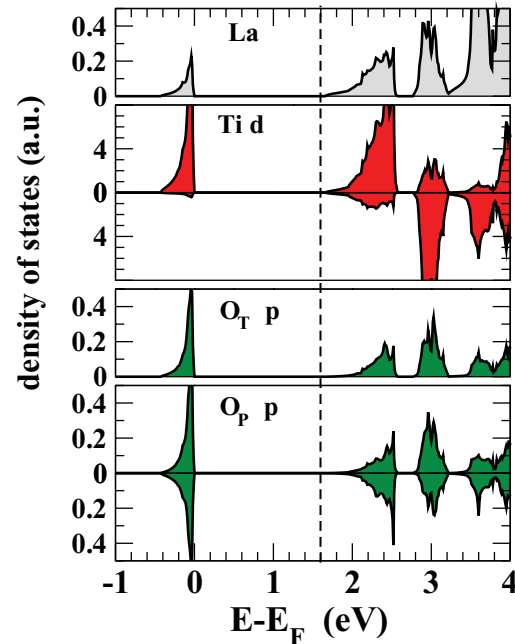
TABLE III. $3d$ orbital decomposition of the four occupied states (one for each Ti) at the VBT of YTO and LTO. The coordinates (x',y',z') and (x,y,z) refer to the orthorhombic and conventional cubic Cartesian axes, respectively, as indicated in Fig. 7.

	$|x'y'\rangle$	$|x'z'\rangle$	$|y'z'\rangle$	$|z'^2\rangle$	$|x'^2 - y'^2\rangle$
YTO					
Ti 1	0.11	0.48	0.58	0.33	0.56
Ti 2	0.11	0.48	−0.58	−0.33	−0.56
Ti 3	−0.11	0.48	0.58	−0.33	−0.56
Ti 4	−0.11	0.48	−0.58	0.33	0.56
LTO					
Ti 1	0.02	0.15	0.78	0.08	0.60
Ti 2	0.02	0.15	−0.78	−0.08	−0.60
Ti 3	−0.02	0.15	0.78	−0.08	−0.60
Ti 4	−0.02	0.15	−0.78	0.08	0.60
	$|xy\rangle$	$|xz\rangle$	$|yz\rangle$	$|z^2\rangle$	$|x^2 - y^2\rangle$
YTO					
Ti 1	0.56	−0.07	0.75	0.33	0.11
Ti 2	−0.56	0.75	−0.07	−0.33	0.11
Ti 3	−0.56	−0.07	0.75	−0.33	−0.11
Ti 4	0.56	0.75	−0.07	0.33	−0.11
LTO					
Ti 1	0.60	−0.45	0.66	0.08	0.02
Ti 2	−0.60	0.66	−0.45	−0.08	0.02
Ti 3	−0.60	−0.45	0.66	−0.08	−0.02
Ti 4	0.60	0.66	−0.45	0.08	−0.02

FIG. 8. (Color online) Orbital-resolved DOS for AF G-type LTO (right). The orbital labels are the same as in Fig. 5. La and O_T states are spin compensated due to the AF G-type symmetry. The La and O DOS scale is magnified by more than one order of magnitude to match the dominant Ti $3d$ DOS.

LTO in the plane, there is a perfect alternance (i.e., chessboard-like order) of the leading $|xz\rangle$ and $|yz\rangle$ contributions (this is less evident than in YTO since the t_{2g} coefficients are not as different as those in YTO), plus a sign alternance for $|xy\rangle$. Along z, only the sign alternance occurs. Our calculated t_{2g} coefficients for LTO (Table III) are again remarkably close to the NMR values (0.56, 0.45, 0.69) from Ref. 30, as well as to those calculated (0.6, 0.39, 0.69) by a model Hamiltonian in Ref. 27.

The observed magnetic ground state is correctly predicted for both materials (in the calculated structure discussed below). For YTO, we found the FM state lower than both the AF-G and AF-C phases by 10.1 and 8.3 meV/f.u., respectively. This is in agreement with previous LDA + U results[37] obtained with $U - J = 3.2$ eV. For LTO, instead, we obtain that the AF-G phase is lower than the FM and AF-A phases by 15.2 and 10.05 meV/f.u., respectively. We then fit our total energies to a two-parameter nearest-neighbor Heisenberg Hamiltonian of the form

$$H = -\frac{1}{2} \sum_i [J_{pl}(\hat{S}_i \cdot \hat{S}_{i+x} + \hat{S}_i \cdot \hat{S}_{i+y}) + J_z \hat{S}_i \cdot \hat{S}_{i+z}], \quad (21)$$

where $i + x$, $i + y$, and $i + z$ indicate the nearest neighbors of the ith atom, respectively, in the x, y, and z directions. We calculate $J_{pl} = 4.15$ meV and $J_z = 1.8$ meV, respectively, for the planar and orthogonal exchange interaction parameters in YTO, while the same quantities for LTO are $J_{pl} = -5.02$ meV and $J_z = -5.03$ meV. These results nicely confirm the conjectures derived by the analysis of the orbital ordering, namely, that, while a remarkable anisotropy is present in YTO, LTO is substantially isotropic.

We now come to discuss the structure of the two titanates. Table IV compares the experimental and VPSIC calculated

TABLE IV. VPSIC-predicted structure of *Pnma* YTO and LTO compared with experiments (in brackets): atomic positions expressed in crystal coordinates $(x/a, x/b, x/c)$ and main structural parameters [Ti-O-Ti angles in the plane (θ_p) and along z (θ_z), Ti-O distances along z (d_z) and in-plane (shorter: d_S, longer: d_L)]. The cell parameters are fixed to the experimental values $a = 5.316$ Å, $b = 5.679$ Å, $c = 7.611$ Å for YTO, and $a = 5.640$ Å, $b = 5.584$ Å, $c = 7.896$ Å for LTO (Ref. 28).

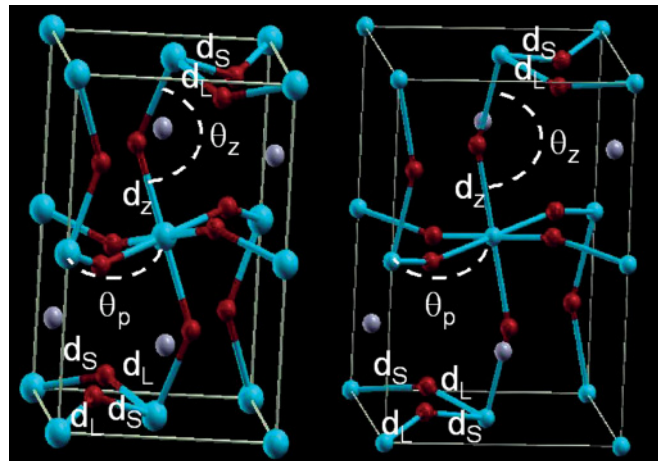|	x/a	y/b	z/c
Y	0.478 (0.479)	0.073 (0.073)	1/4
Ti	0	0	1/2
O$_I$	−0.139 (-0.121)	−0.063 (−0.042)	1/4
O$_{II}$	0.307 (0.309)	0.184 (0.190)	0.067 (0.058)
La	0.491 (0.493)	0.053 (0.043)	1/4
Ti	0	0	1/2
O$_I$	−0.080 (−0.081)	−0.008 (−0.007)	1/4
O$_{II}$	0.0288 (0.291)	0.204 (0.206)	0.042 (0.043)
	d_S	d_L	d_z
YTO	2.0 (2.02)	2.13 (2.08)	2.07 (2.02)
LTO	2.02 (2.03)	2.06 (2.05)	2.02 (2.03)
	θ_p	θ_z	
YTO	140.41° (143.62°)	133.30° (140.35°)	
LTO	153.82° (152.93°)	154.30° (153.75°)	

FIG. 9. (Color online) *Pnma* structure of YTO (left) and LTO (right). The cell parameters are fixed to experimental values, while atomic positions are relaxed according to the VPSIC method. The labels indicate Ti-O-Ti angles and Ti-O distances in plane (θ_p, d_p) and along z (θ_z, d_z). The numerical values of the various structural parameters are reported in Table IV.

internal atomic coordinates and the most important structural parameters, namely, the Ti-O-Ti angles (θ) and the Ti–O distances (see also Fig. 9). The VPSIC calculated structure is very close to the experimentally determined one for both LTO and YTO (although, for the latter, the oxygen rotations are slightly overemphasized along the z axis). There are two types of in-plane Ti–O bonds, long (d_L) and short (d_S), which alternate along both x and y (see Fig. 9), while along z, there is only one, $d_z \sim d_S$. This gives an easy rationale for the chessboardlike Ti d ordering: on each Ti atom, the occupied state prefers to lie along the longer Ti–O bond (thus, alternatively $|xz\rangle$ and $|xy\rangle$ for d_L parallel to x, or $|yz\rangle$ and $|xy\rangle$ for d_L parallel to y). For YTO, the difference between d_L and d_S is quite substantial and give rises to a very pronounced ordering, as seen in the analysis of the charge density. For LTO, the d_L and d_S difference is much reduced and it results in a planar chessboard ordering.

For both materials, the large GdFeO$_3$-type distortion is the main factor determining the observed structures and the consequent splitting of the t_{2g} triplet state. The Jahn-Teller distortions are instead small (i.e., the properties along x, y, and z are similar, on average, especially for LTO). Remarkably, our method predicts these subtle but important details with great accuracy.

An issue that still remains to be clarified is the large difference between the calculated and the measured energy gaps. This is particularly dramatic in LTO [over 1 eV against around 0.1 eV (Ref. 35)] and it is a problem shared by all *ab initio* methods. Such a problem, however, lies in a confusion about the actual definition of the gap. In fact, the VBT and CBB band energies are approximations to removal and addition energies, and their difference estimates the onsite Coulomb energy U. In contrast, the lowest-energy electronic excitation measured for these true Mott-Hubbard insulators is very likely an intrasite, intra-t_{2g} excitation, which of course does not involve any U. Inferring a small effective U from the tiny measured (direct forbidden) gap[35] of LaTiO$_3$ is

then a misinterpretation. According to our band structure, U is in the order of approximately 3 eV, as expected for a system of this kind. In fact, similar values have been used in LDA + U and DMFT calculations. It is also not very convincing to estimate the intrasite excitation energy from the LDA calculated t_{2g} (average) band splitting. The result may be deemed plausible since excitation and addition or removal energies become identical in the limit of vanishing U (i.e., delocalized electrons). However, here a vanishing U is an artifact of the LDA and not a true feature of the titanate. A better grounded strategy, suggested in Ref. 38, constructs a Hamiltonian for the excited state explicitly by projecting out the electronic ground state (an approach beyond our present methodological scope).

In summary, the VPSIC approach provides a coherent understanding of YTO and LTO, of their relevant differences in terms of structure, magnetism, orbital ordering, and charge decomposition. The larger $GdFeO_3$-type distortion of YTO results in a larger Ti $3d$-O $2p$ and t_{2g}-e_g mixing, larger occupied $3d$ state bandwidth, and crucially different charge density distribution around Ti. The wider the rotations, in particular, the stronger is the destabilization of the AF superexchange coupling, which otherwise would prevail in a purely d^1 t_{2g} unrotated *Pnma* environment.

Note that the connection between structural and electronic and magnetic properties would be completely reverted for doped manganites, the chemistry of which is governed by the e_g orbitals. In that case, the cubic symmetry and the absence of octahedral rotations work in favor of an e_g-p hybridization. Conversely, in titanates, the absence of octahedral rotations implies vanishing p-d hybridization, pure t_{2g} charge character, and minimal t_{2g} bandwidth.

Finally, it is worth noticing the good quantitative agreement of the orbital ordering predicted by VPSIC with that obtained in LDA + DMFT (Ref. 39). More in general, in a relevant number of strong-correlated materials, the description by the VPSIC approach (or its predecessor PSIC-ASIC) of electronic and magnetic properties is found in very good agreement with theories that include dynamical effects.

While the importance of dynamical corrections in the general case is undeniable, we emphasize that a sound quantitative estimate of the dynamical corrections can not leave aside the error proper of the static limit with respect to which they are evaluated. Thus, we may argue that the role of dynamical effects may be overemphasized if the LDA, or even LDA + U, are taken as reference static limit. On the other hand, the VPSIC approach, which we regard as a more accurate static limit than LDA or LDA + U, might even consent a better evaluation of dynamical effects. To this aim, it is obviously instrumental in the implementation of the VPSIC + DMFT approach, an achievement that indeed stands in our future plans.

C. Magnetic manganites: CaMnO₃

As a further example of the capability of the VPSIC approach in describing solids, we consider the prototypical AF G-type insulator $CaMnO_3$ (CMO) as representative of magnetic manganites. The nominal Mn^{4+} d^3 configuration triggers the AF superexchange coupling via the fully polarized majority t_{2g} orbitals and an AF semicovalent exchange interaction through

the empty e_g states. The t_{2g} spherical charge distribution favors a robust centrosymmetric octahedral structure, and the near complete absence of rotations leaves the systems substantially cubic (a small *Pnma* distortion is actually observed, but it will not be considered here since it is immaterial for the magnetic and electronic properties). According to the Goodenough-Kanamori rules,[45] the spin coupling is expected to be AF and isotropic (G type). While this is indeed verified by a series of experiments and calculations, a detailed determination of the electronic and magnetic properties is less clear, and some discrepancies between the interpretation of photoemission data and band energies obtained with standard local functionals make the system an interesting test case for our methods. Indeed, from the theoretical side, CMO was studied in the past by using LDA,[46–50] GGA,[51] LDA + U,[47] GGA + U,[52] unrestricted Hartree-Fock (HF),[53,54] configuration interaction (CI),[54] and model (Hubbard) Hamiltonian.[55] At the same time, experimentally, a number of optical[56–58] and transport[59] measurements have been carried out.

The general electronic characteristics of CMO can be illustrated with the help of our calculated DOS (Fig. 10) and band energies (Fig. 11) for the observed AF G-type phase at the experimental lattice parameter. All levels of theory (LDA, VPSIC, and VPSIC₀) describe the system as an insulator, with a ∼7-eV-wide valence-band manifold of mixed O p and majority Mn d t_{2g} states. Very importantly, at variance with the nominal configuration, a consistent amount of filled e_g states is present in all the three calculated DOS. At about 18 eV below the p-d valence bands lies a narrow, mostly O $2s$, manifold. Above the fundamental gap, we find distinct groups of majority e_g, minority t_{2g}, and minority e_g states.

By looking closer at the DOS, important differences appear in the LSDA and VPSIC and VPSIC₀ descriptions. For both computational schemes, the p-d valence manifold shows a double-peaked structure, in agreement with x-ray photo-electron spectroscopy (XPS) and ultraviolet photoemission
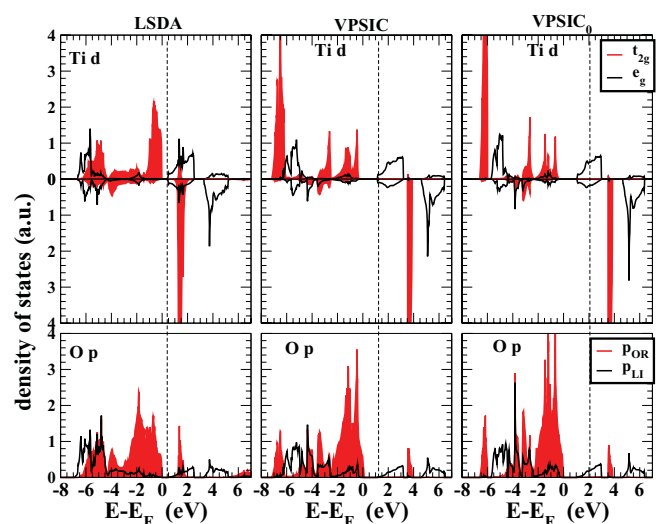

FIG. 10. (Color online) Density of states of the most important orbitals (Mn d and O p) of AF-G CMO calculated within LDA, VPSIC, and VPSIC₀. Light (red) shadowed areas are for Mn t_{2g} and O p orthogonal orbitals; solid black lines for Mn e_g and O p ligand orbitals.
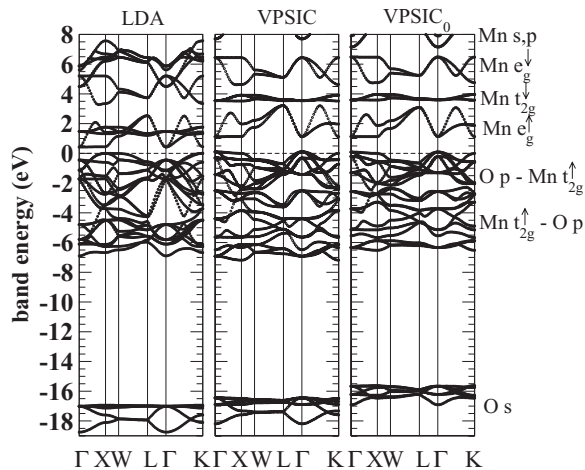
FIG. 11. Band energies of AF-G type CMO in the cubic fcc symmetry, calculated with LSDA, VPSIC, and $VPSIC_0$. The k-point coordinates (units of $2\pi/a$) are $\Gamma = [0,0,0]$, $X = [1,0,0]$, $W = [1,1/2,0]$, $L = [1/2,1/2,1/2]$, $K = [1,1,0]$. The dominant and secondary orbital character for each group of bands is also indicated.

FIG. 12. (Color online) Total energies per cell as a function of the lattice parameter calculated by LSDA, VPSIC, and $VPSIC_0$ for the AF-G (solid symbols) and FM (open symbols) ordering. The differences in total energy between the different methods have no physical meaning, and the curves are arbitrarily translated vertically for the sake of clarity.

spectroscopy (UPS),[56] but the orbital character of the peaks is different: in LSDA, most of t_{2g} spectral weight is right below the VBT, while the tail region from –5 to –7 eV is mainly O $2p$. In contrast, the VPSIC and $VPSIC_0$ recover a spectral redistribution more in line with the experimental observations, with prevalently O $2p$ states near VBT and the highest peak of t_{2g} states at the bottom of the valence bands. The LSDA inaccuracy is clearly related to an insufficient t_{2g} spin splitting, which amounts to a mere 2.5 eV and leaves the majority t_{2g} much too high in the energy. In the VPSIC approach, the t_{2g} splitting increases up to about 9 eV, which is consistent with the estimated U.[55] Notably, a single energy parameter is actually not enough to properly locate the t_{2g} states since a consistent portion thereof is also present in the 4-eV-wide region below the VBT, where the p-d hybridization is strong.

In LSDA, we obtain an energy band gap of 0.42 eV. By looking at the band picture (Fig. 11), the VBT runs flat between X and W, while the CBB e_g is flat between Γ and X, in agreement with previous LDA calculations (see, e.g., Ref. 49). In the VPSIC approach, the gap is now 1.01 eV, and both VBT and CBB are flat between Γ and X. Above the energy gap, LSDA describes the 2-eV-wide majority e_g bands overlapped with the very narrow minority t_{2g} peak, whereas in VPSIC and $VPSIC_0$, the latter lies about 2 eV above the centroid of the e_g. Although we could not find in literature a clear determination of the band-gap value, interband transitions extracted from photoemission[57] and optical conductivity measurements[56] seem to be very consistent with the VPSIC calculations. Specifically, the distance between O $2p$ and the majority e_g peaks (~3 eV) and between O $2p$ and the minority e_g peak (~6.5 eV) compare well with the respective values 3.07 and 6.49 eV extracted by Lorentz oscillator fitting of the conductivity spectra (Ref. 56). Also quite consistent, albeit with a slightly larger value (3.7 eV) for the O $2p$-Mn e_g transition, is the valence-band spectra deduced in Ref. 57 by fitting a CI cluster model to XPS data.
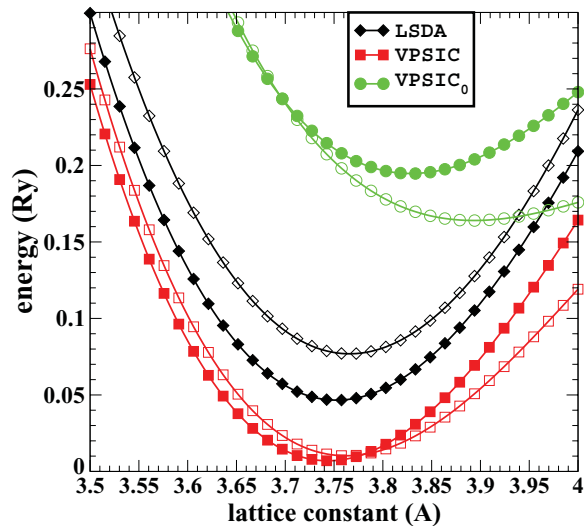
Next, we move to examine the structural and magnetic properties. Figure 12 reports the total energies calculated with LSDA, VPSIC, and $VPSIC_0$ as a function of lattice parameter for both the AF-G and FM CMO phases. The values of the equilibrium lattice are reported in Table V. The trend is similar to that seen already in Sec. III A for wide-gap oxides: VPSIC and $VPSIC_0$, respectively, reduce and expand the volume with respect to the LSDA. Here, however, the VPSIC correction is tiny and both the LSDA and VPSIC approach give lattice constants rather close (within 1%) to experiments. In contrast, the $VPSIC_0$ is much less satisfying and overestimates the lattice constant by ~2.5%.

Concerning the difference of AF-G and FM energies, LSDA is known to overestimate the contribution of the AF superexchange due to the excessive t_{2g}-p hybridization in the region near VBT (as discussed in Fig. 10), thus, it predicts a strong AF-G stability (in agreement with previous[40,46] LSDA calculations) through the entire examined range of lattice parameters. The VPSIC approach, in contrast, suggests a much tighter competition: while at equilibrium, the AF-G phase is stable, a moderate lattice stretching (a tensile strain of about 1%) is sufficient to reverse the magnetic order and stabilize

TABLE V. Equilibrium lattice parameter a_0 (in Å) for the AF-G and FM phases and exchange interaction J (in meV) for cubic $CaMnO_3$ calculated by LSDA, VPSIC, and $VPSIC_0$ (experimental values are reported for comparison). J_{eq} and J_{ex} are values calculated for equilibrium and experimental a_0, respectively.

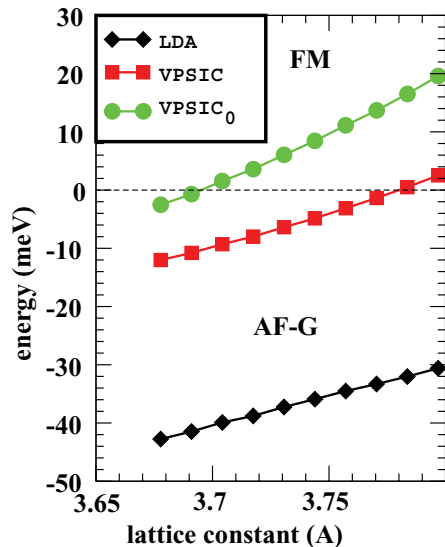|	LSDA	VPSIC	$VPSIC_0$	Expt.
a_0 (AF-G)	3.75	3.74	3.83	3.734
a_0 (FM)	3.77	3.76	3.88	
J_{ex}	−37.0	−6.1	+6.5	−6.6 (Ref. 60)
J_{eq}	−35.3	−5.7	+27.3	

FIG. 13. (Color online) Exchange-interaction parameter J calculated with LSDA, VPSIC, and VPSIC$_0$; see text for the exact definition of J.
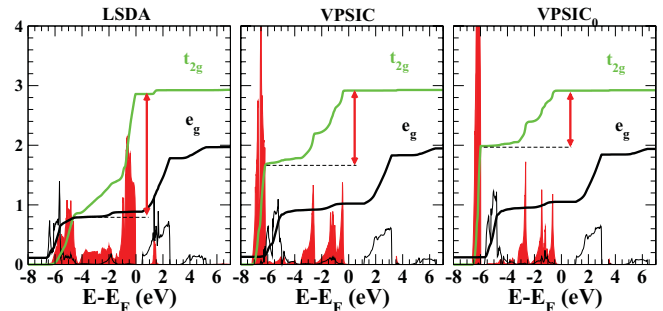

FIG. 14. (Color online) Integrated DOS of t_{2g} (green) and e_g (black) majority orbitals, normalized to their respective degeneracies 3 and 2. The DOS are also reported for clarity. The length of red arrows indicate the amount of t_{2g} charge without the lowest t_{2g} peak.

the FM ground state. Finally, the VPSIC$_0$ apparently performs very poorly for magnetic coupling: it completely reverses the LSDA description and predicts the FM as the stable phase in a wide lattice constant range.

The magnetic competition can be better appreciated in terms of exchange-interaction parameters J, plotted in Fig. 13. For the sake of comparison, we have adopted the same definition of J given in Ref. 54, which is based on the single-parameter Heisenberg Hamiltonian

$$H = -J \sum_{ij} \hat{e}_i \cdot \hat{e}_j,$$

where $\hat{e}_i$ is the unit vector of the i-site spin direction. Values calculated at equilibrium (J_{eq}) and experimental (J_{ex}) lattice constant are reported in Table V. We remark here the excellent agreement of the VPSIC value of –6.1 meV with $J = -6.6$ meV extracted from the diagrammatic Rushbrooke-Wood formula[60] for the magnetic susceptibility corresponding to the experimental Néel temperature $T_N = 130$ K. The VPSIC approach also compares fairly well with those calculated by CI (8.1 meV) and HF (10.7 meV) in Ref. 54. This contrasts with both the LSDA and VPSIC$_0$ values, which largely deviate from these estimates, albeit in opposite directions.

It is interesting to speculate on the remarkably different magnetic behavior described by the three methods. This mainly reflects the difference in the t_{2g} spectral weight seen in Fig. 10, specifically, the substantial DOS shift from the top to the bottom of the p-d band manifold when moving from LSDA to VPSIC and to VPSIC$_0$. In order to quantify this effect, in Fig. 14, we report the integrated charge for the majority t_{2g} and e_g bands as described by the three methods. The e_g charge integrates to a remarkable 1/2 electron per orbital at the VBT (in agreement with previous calculations[52]) and it contributes to the FM coupling via e_g-p hybridization according to the Goodenough-Kanamori rules.[45] On the t_{2g} side, all the methods describe filled (i.e., with a total integral of 3) t_{2g} DOS. However, if we evaluate the amount of t_{2g} charge located

in the upper part of the valence-band region, which does not include the towering lower-end peak and mainly hybridizes with oxygens (quantified in Fig. 14 by the vertical red arrows), we find that this charge in LSDA is about 73%, in VPSIC just 43%, and finally in VPSIC$_0$ a mere 33% of the entire majority t_{2g} charge. Our interpretation is then the following: when going from LDA to VPSIC to VPSIC$_0$, the t_{2g} spectral weight is progressively transferred toward the lower end of the valence band. Its hybridization with oxygen decreases and so does the superexchange AF contribution (through t_{2g}-p π-type bonding). The e_g charge distribution, instead, remains substantially unchanged in the three methods, so that the FM contribution increases as compared to AF superexchange from weak in LDA to competitive in VPSIC to dominant in VPSIC$_0$.

In summary, the VPSIC approach provides a very consistent description of the electronic, structural, and magnetic properties of CMO. VPSIC calculated values compare well with the experiments and with results of other beyond-local approaches, i.e., the most obvious deficiencies of the LSDA are corrected. This is not the case for VPSIC$_0$. In fact, while it offers a band spectrum substantially similar to that of the VPSIC approach, it fails in the precise account of structural and magnetic properties. Our study has revealed that subtle differences in the electronic properties can result in visible errors in some observable quantities. Specifically, a slightly narrower p-d valence bandwidth and an excessive t_{2g} localization toward the lower end of the valence-band manifold can result in a 2%–3% overestimation of the lattice constant and in an unreliable value of the exchange-interaction parameter.

IV. RESULTS: MOLECULES

While the PSIC approach was originally formulated for extended solids (i.e., for periodic boundary conditions), it may be just as useful for finite systems. Indeed, the full PZ-SIC is easy and straightforward for isolated atoms, but for large molecules, clusters, or complex structures such as molecular contacts, its application may become cumbersome and expensive, when not outright impossible. The PSIC approach provides a practical and reliable alternative. The implementation within local orbital basis set and pseudopotentials (ASIC), carried out in Ref. 5 in the framework of the SIESTA code,[6] can treat both extended and finite systems on the same footing (of course, in principle, the plane-wave implementation can be applied

to finite systems via a supercell approach, albeit much less efficiently). In the last few years, a series of works related to molecules have been carried out by the ASIC approach (Refs. 61–65) with typically satisfactory results (provided that the relaxation parameter α is kept fixed to unity). The VPSIC approach implemented in local orbital basis set (i.e., the variational generalization of the ASIC) is expected to yield KS spectra largely similar, although not identical, to those obtained with ASIC. Additionally, the performance of the VPSIC energy functional [Eq. (1)] and the associated forces [Eq. (19)] for equilibrium molecular geometries need to be investigated.

In this section, we look at the VPSIC description of the spectral and geometric properties of several molecules selected mostly, but not exclusively, from the standard G2 set.[66] Calculations are carried out using a development version of the SIESTA code[6] within which the VPSIC method was implemented. Some details regarding the implementation are given in Appendices C and D. For all of the atomic species, standard norm-conserving pseudopotentials generated by using the Troullier-Martins scheme[67] are employed including core corrections where necessary. Scalar relativistic pseudopotentials are used for the period III elements. A numerical double-zeta-polarized (DZP) basis set[6] is employed for all of the atomic species, and an energy shift of 50 meV is used to set the cutoff radius for the pseudoatomic orbital (PAO) basis functions. Geometry optimizations are performed by using a conjugate gradients algorithm until all of the forces are smaller than 0.01 eV/Å.

A. Equilibrium bond lengths

Table VI shows the equilibrium bond lengths obtained within the VPSIC approach for selected bonds in several gas phase molecules. The representative set chosen includes molecules mainly built from I, II, and III period elements as well as nonmagnetic transition metals. Furthermore, it includes several species hosting different types of chemical bonds. Also presented for comparison are the corresponding LSDA and experimental bond lengths. We find that the calculated VPSIC bond lengths are generally shorter than the corresponding LSDA estimates. From column 5 in Table VI, we see that the LSDA bond lengths are typically a few percent longer than in experiments, while (see column 4 in Table VI) those of the VPSIC are seen to be a few percent shorter. In columns 6 and 7, we show the absolute percentage error

$$\delta_{\mathrm{BL}}^i(X) = \frac{\left| L_i(X) - L_i^{\mathrm{expt}} \right| \times 100}{L_i^{\mathrm{expt}}}$$

in the calculated bond lengths $L_i(X)$ relative to the experimental ones L_i^{expt} for each of the molecular species i and $X \in$ {VPSIC, LSDA}. The estimated mean absolute percentage error over the test set

$$\Delta_{\mathrm{BL}}(X) = \frac{\sum_{i=1}^N \delta_{\mathrm{BL}}^i(X)}{N}$$

comes out to be 1.84% in LSDA and 1.77% in VPSIC. We also note further that, within the test set, the maximum percentage error observed within VPSIC is ∼4% for the case of the Z–H bond in ZnH and that for the majority of the molecules the error

is typically under 2.0%. Interestingly, we find that the VPSIC considerably worsens over the LSDA bond lengths for single covalent bonds between identical atoms (see, for instance, C_2H_6, C_4H_8, C_3H_6, O_3), while it significantly improves them when the bond is either double (C_2H_4, CO, CO_2, O_2) or triple (N_2 and C_2H_2). For other bonds between nonidentical atoms, the results are mixed.

In summary, as previously found for solids, also for molecules the VPSIC yields structural properties of rather similar quality to those calculated with the LSDA. In this case, however, for most of the molecules investigated, we found the VPSIC approach to overcorrect the LSDA, so that although the errors are similar, they have the opposite signs.

B. Ionization potentials

As in the case of the ASIC method, the primary advantage over LSDA afforded by the VPSIC method is expected to lie in the systematic improvement of KS eigenvalue spectra as approximate proxies for addition and removal energies. The method is particularly relevant for DFT-based transport theory, where an accurate description of the KS spectra[68,69] is important. In exact KS DFT, only the highest occupied orbital eigenvalue (ϵ^{HOMO}) has a rigorous physical interpretation and corresponds to the negative of the first ionization potential.[70,71] In general, for an N electron system, the following equations hold in exact KS DFT:

$$\epsilon^{\mathrm{HOMO}}(M) = -I_N \, \mathrm{for} \, (N - 1 < M \leqslant N), \quad (22)$$

$$\epsilon^{\mathrm{HOMO}}(M) = -A_N \, \mathrm{for} \, (N < M \leqslant N + 1), \quad (23)$$

where $-I_N$ and $-A_N$ are the ionization potential (IP) and the electron affinity (EA), respectively. However, local and semilocal functionals such as the LSDA and GGA are known to perform poorly at satisfying the equations (22) and (23), particularly for molecular systems. In the following, we assess the mapping between electron removal or addition energies and the KS spectrum obtained from the VPSIC approach, also showing the corresponding LSDA results for comparison. Furthermore, for both LSDA and VPSIC, the molecular geometries used to estimate the IP and EA are the corresponding equilibrium geometries in the neutral configuration.

In Table VII and Fig. 15, we compare the experimental IP for several molecules with the corresponding negative ϵ^{HOMO} obtained by using either the LSDA or VPSIC approach. It is clear that LSDA underestimates the removal energies significantly in all the cases. In contrast, the mapping between the experimental IP and $-\epsilon^{\mathrm{HOMO}}$ from the VPSIC approach is excellent. In this case, the mean absolute deviation from experiment

$$\Delta_{\mathrm{IP}}(X) = \frac{\sum_{i=1}^M \left| \epsilon^{\mathrm{HOMO},i}(X) + \mathrm{IP}_{\mathrm{expt}}^i \right|}{M},$$

with ($X = $ LSDA, VPSIC), is estimated to be 4.29 eV for LSDA and 0.72 eV for VPSIC (M is the total number of molecules in Table VII). For comparison, we have also included in Fig. 15 results obtained with a fully self-consistent PZ-SIC approach.[72] Somewhat surprisingly, the VPSIC approximation seems to produce better overall agreement with experiments than the full PZ-SIC scheme, which is seen to overcorrect the energy levels. This is a rather general feature of the

TABLE VI. Calculated bond lengths of selected bonds from several molecules compared to experimental values. Both VPSIC and LSDA bond lengths are shown. δ_{BL} in column 6 (7) denotes the absolute percentage difference between the calculated VPSIC (LSDA) and experimental bond length.

Molecule	Bond	Bond length (Å)			$\delta_{BL}(\%)$	
		VPSIC	Experiment	LSDA	VPSIC	LSDA
BCl_3	B–Cl	1.748	1.742	1.754	0.349	0.706
CH_4	C–H	1.081	1.087	1.121	0.567	3.090
C_2H_6 (ethane)	C–C	1.478	1.536	1.524	3.751	0.776
C_4H_8 (cyclobutane)	C–C	1.503	1.555	1.548	3.315	0.419
C_3H_6 (cyclopropane)	C–C	1.471	1.501	1.519	1.986	1.168
O_3	O–O	1.224	1.278	1.273	4.200	0.364
NaCl	Na–Cl	2.317	2.361	2.336	1.883	1.039
SiH_4	Si–H	1.431	1.480	1.518	3.344	2.594
$SiCl_4$	Si–Cl	2.020	2.019	2.054	0.056	1.747
PH_3	P–H	1.407	1.421	1.460	0.997	2.736
PF_3	P–F	1.576	1.561	1.644	0.957	5.349
SH_2	S–H	1.341	1.328	1.382	0.984	4.030
CuF	Cu–F	1.763	1.745	1.735	1.009	0.548
ZnH	Zn–H	1.527	1.595	1.629	4.260	2.130
C_2H_4 (ethylene)	C = C	1.309	1.339	1.351	2.237	0.903
CO	C = O	1.124	1.128	1.153	0.384	2.217
CO_2	C = O	1.142	1.162	1.185	1.706	1.959
O_2	O = O	1.188	1.210	1.227	1.793	1.388
N_2	N≡N	1.086	1.098	1.119	1.077	1.924
C_2H_2 (acetylene)	C≡C	1.196	1.203	1.234	0.566	2.605
C_6H_6 (benzene)	C:C	1.371	1.397	1.411	1.871	0.985
Δ_{BL}					1.77	1.84

PZ-SIC scheme, and it has been suggested that some additional rescaling procedure is needed.[73,74]

C. Electron affinities and the HOMO-LUMO gap

In Hartree-Fock theory, Koopmans' theorem[76] implies that the lowest unoccupied molecular orbital (LUMO) energy (ϵ^{LUMO}) corresponds to the EA of the N electron system
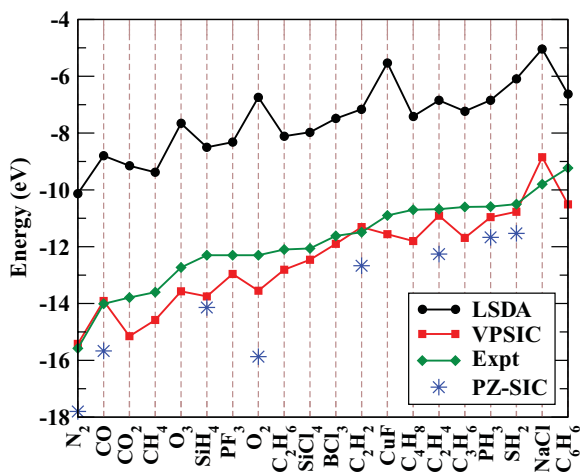

FIG. 15. (Color online) Experimental negative ionization potential IP compared to the calculated HOMO eigenvalues for molecules. The experimental data are from Ref. 75, while the star symbol represents full PZ-SIC calculations from Ref. 72.

TABLE VII. Experimental ionization potential (IP) compared to the calculated negative HOMO eigenvalues for neutral molecules. Columns 2 and 3 present the results from LSDA and VPSIC, respectively. The experimental data are taken from Ref. 75.

| Molecule	$-\epsilon^{HOMO}$ (eV)		IP (eV)
	LSDA	VPSIC	Experiment
BCl_3	7.49	11.90	11.62
CH_4	9.38	14.58	13.60
C_2H_6 (ethane)	8.11	12.81	12.10
C_4H_8 (cyclobutane)	7.41	11.80	10.70
C_3H_6 (cyclopropane)	7.23	11.69	10.60
O_3	7.66	13.57	12.73
NaCl	5.04	8.85	9.80
SiH_4	8.50	13.75	12.30
$SiCl_4$	7.97	12.46	12.06
PH_3	6.84	10.96	10.59
PF_3	8.32	12.96	12.30
SH_2	6.09	10.77	10.50
CuF	5.53	11.56	10.90
C_2H_4 (ethylene)	6.85	10.91	10.68
CO	8.80	13.91	14.01
CO_2	9.15	15.15	13.79
O_2	6.74	13.55	12.30
N_2	10.13	15.42	15.58
C_2H_2 (acetylene)	7.16	11.31	11.49
C_6H_6 (benzene)	6.63	10.51	9.23
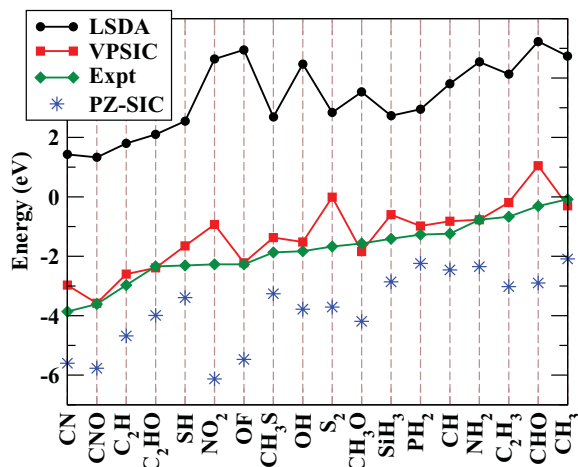
FIG. 16. (Color online) Experimental negative electron affinities ($-$EA) compared to calculated HOMO eigenvalues of negative radicals.

when electronic relaxation is neglected. No such physical interpretation exists for the Kohn-Sham (ϵ^{LUMO}) in DFT and so the EA is not directly accessible from the ground-state spectrum of the N electron system. However, as Eq. (22) indicates, the EA is, in principle, accessible from the ground-state spectrum of the $N + 1 - f$ ($0 < f < 1$) electron system and, furthermore, it must be relaxation free through noninteger occupation. Approximate functionals such as the LSDA and GGA, however, perform rather poorly even in this regard as the $N + 1$ electron state is often unbound with a positive eigenvalue. Therefore, in practice, electron affinities are usually extracted either from more accurate total energy differences[77] or by extrapolating them from LSDA calculations for the N electron system.[78] The failure of approximate functionals in reproducing the spectra of anions has been traced for the largest part to the SI error; SIC schemes are expected to perform better in this regard.

In Table VIII, we compare the HOMO energies (denoted as $\epsilon_{N+1}^{\text{HOMO}}$) of several singly negatively charged molecules with the experimental electron affinities of the corresponding neutral species. We also report the LUMO energies for the molecules, most of which are radicals, in their neutral ground state (denoted as ϵ_N^{LUMO}). Relaxed geometries of the neutral molecule are used for both the neutral and charged cases. We find that various $-\epsilon_{N+1}^{\text{HOMO}}$ obtained from the VPSIC approach once again map quite well onto the corresponding experimental electron affinities in contrast to LSDA, which yields unbounded states with positive $\epsilon_{N+1}^{\text{HOMO}}$ for all the systems considered. Over the set of molecules in Table VIII, the mean absolute error with respect to experiment for the electron affinities

$$\Delta_{\text{EA}}(X) = \frac{\sum_{i=1}^{N} \left| \epsilon_{N+1}^{\text{HOMO,i}}(X) + \text{EA}_{\text{expt}}^{i} \right|}{N} \qquad (24)$$

(X = LSDA, VPSIC) stands at 4.67 and 0.54 eV for LSDA and VPSIC, respectively. In Fig. 16, we present our data together with $\epsilon_{N+1}^{\text{HOMO}}$ as calculated using the PZ-SIC.[72] For the electron affinities as well, we see that the PZ-SIC seems to systematically overcorrect the LSDA shortfall.

TABLE VIII. Calculated HOMO eigenvalues for singly negatively charged molecules compared to the experimental negative electron affinities ($-$EA). Columns 6, 7, and 8 present the LUMO eigenvalues for the corresponding neutral species. Experimental values for the electron affinities are taken from Ref. 72.

Molecule	$\epsilon_{N+1}^{\text{HOMO}}$ (eV)			ϵ_N^{LUMO} (eV)	
	LSDA	VPSIC	Expt. $-$EA (eV)	LSDA	VPSIC
HC≡C$^-$	1.79	-2.60	-2.97	-6.54	-7.59
CH$_2$=CH$^-$	4.13	-0.19	-0.67	-3.49	-5.07
HC≡CO$^-$	2.09	-2.39	-2.34	-5.98	-8.08
CH$^-$	3.80	-0.82	-1.24	-4.81	-7.15
CH$_3^-$	4.73	-0.30	-0.08	-3.39	-3.41
CH$_3$O$^-$	3.52	-1.84	-1.57	-5.53	-6.15
CH$_3$S$^-$	2.68	-1.37	-1.87	0.3	-5.73
HC=O$^-$	5.22	1.05	-0.31	-3.36	-6.86
CN$^-$	1.42	-2.97	-3.86	-7.83	-10.82
CNO$^-$	1.32	-3.58	-3.61	-0.62	-4.16
NH$_2^-$	4.54	-0.77	-0.77	-4.98	-4.33
NO$_2^-$	4.64	-0.93	-2.27	-5.02	-9.47
OF$^-$	4.95	-2.22	-2.27	-2.16	-6.14
OH$^-$	4.46	-1.52	-1.83	0.44	-1.86
PH$_2^-$	2.94	-0.98	-1.27	-4.55	-4.99
S$_2^-$	2.83	-0.01	-1.67	-4.5	-6.67
SH$^-$	2.54	-1.65	-2.31	-0.17	-2.72
SiH$_3^-$	2.72	-0.60	-1.41	-3.85	-5.38

We now discuss briefly the HOMO-LUMO gap in the VPSIC approach. As it is apparent from columns 5 and 6 in Table VIII, the LUMO eigenvalues of the neutral species differ substantially from the corresponding negative electron affinities both within the LSDA and VPSIC approach. In general, DFT LUMO states are expected to be lower than $-$EA by an amount equal to the derivative discontinuity Δ_{xc} defined as

$$\Delta_{\text{xc}} = \lim_{f \to 0^+} \epsilon_{N+f}^{\text{HOMO}} - \epsilon_N^{\text{LUMO}}, \qquad (25)$$

i.e., Δ_{xc} is the discontinuity in the eigenvalue of the LUMO state at N. Thus, the HOMO-LUMO gap is usually underestimated with respect to the true quasiparticle gap $E_g = I_N - A_N$. In Table IX, we compare the HOMO-LUMO gaps from LSDA and VPSIC calculated in the neutral configuration for the molecular test set of Table VII. We see that, although the VPSIC HOMO eigenvalues are generally significantly lower than those of the corresponding LSDA (see Table VII), the HOMO-LUMO gaps differ by a smaller extent. This is because, in contrast to other methods, such as LSDA + U (Ref. 79), wherein the occupied levels are pushed lower and the unoccupied ones are pushed higher relative to the LSDA spectrum, within the VPSIC approach, the entire spectrum is lowered, with the occupied and empty levels being shifted by different amounts depending upon their orbital character. For instance, the mean absolute difference between the LSDA and VPSIC HOMO-LUMO gaps for the test set in Table IX comes out to be ~2.52 eV, while the correction to the HOMO levels alone with respect to LSDA is around 4 eV. In general, the VPSIC method is expected to open the HOMO-LUMO gap substantially in systems where the occupied and unoccupied KS eigenstates have markedly

TABLE IX. Calculated HOMO-LUMO gaps (E_g) of neutral molecules from LSDA and VPSIC. δE_g in column 4 represents the difference between corresponding VPSIC and LSDA gaps.

Molecule	E_g		δE_g
	LSDA	VPSIC	
BCl_3	4.84	6.76	1.92
C_6H_6 (benzene)	5.33	6.17	0.84
C_2H_2 (acetylene)	6.61	8.27	1.66
C_2H_4 (ethylene)	5.58	6.99	1.41
C_2H_6 (ethane)	9.03	11.64	2.61
CH_4	10.63	13.79	3.16
CO	6.62	9.41	2.79
CO_2	8.33	11.03	2.7
CuF	1.5	6.93	5.43
C_4H_8 (cyclobutane)	8.13	10.29	2.16
C_3H_6 (cyclopropane)	8.15	10.38	2.23
N_2	7.97	10.27	2.3
$NaCl$	2.9	6.75	3.85
O_2	2.16	5.55	3.39
O_3	1.67	3.23	1.56
PF_3	6.26	9.11	2.85
PH_3	6.63	8.47	1.84
SH_2	5.62	8.0	2.38
$SiCl_4$	5.89	7.79	1.9
SiH_4	8.64	12.01	3.37
TiO_2	1.51	4.01	2.5

different atomic-orbital projections. Finally, it is worth noting that, in contrast to explicitly orbital-dependent methods such as PZ-SIC, the VPSIC approach does not exhibit the derivative discontinuity at integer occupations. The eigenvalue of the highest occupied orbital relaxes continuously across fractional occupations; the range of eigenvalue relaxation is generally much smaller than in LSDA.

In summary, as for the solids, also our results for molecules appear very encouraging. In general, our approach formulated in the VPSIC method preserves intact the already satisfactory electronic structure of molecules calculated with ASIC. In addition, the geometries are at least at the LSDA level, and in many cases, even better. Although a much more extensive analysis needs to be carried out to achieve a fully quantitative benchmark, we can already conclude positively on the capability of the VPSIC method to describe on the same footing both structural and electronic properties of molecules. Given the lightweight computational overheads associated to the VPSIC method implemented in SIESTA, we believe that our approach might become extremely attractive for problems where one has to compute single-particle levels for large systems. An example of this can be the problem of determining the level alignment of molecules on surfaces or electron transport in molecular junctions.

V. CONCLUSIONS

In conclusion, we have introduced the first-principles VPSIC approach, a variational generalization of the method formerly known as PSIC and ASIC. This is based on the idea of removing the spurious self-interaction from the local density functional energy. In the VPSIC approach, the self-interaction

is removed in an effective albeit approximate (i.e., orbitally averaged) manner, which gives several advantages over the full SI removal (applied, for example, in the PZ-SIC approach or in related methods for extended systems). In particular, the method conserves translational invariance (i.e., Bloch theorem) in solids and the total energy is invariant under unitary rotations of the occupied KS eigenfunction manifold. The VPSIC approach emerges as applicable to a vast series of systems (insulators and metals, magnetic and nonmagnetic, extended or finite) with an overall satisfactory accuracy. Furthermore, it is not more demanding than LDA and GGA from a computational viewpoint.

We have implemented the method in two numerical frameworks, namely, plane-wave basis set and ultrasoft pseudopotentials, and local orbital basis set plus norm-conserving pseudopotentials. The former scheme was applied here to extended systems (nonmagnetic oxides, magnetic titanates, and magnetic manganites), the latter to a vast range of molecules. In both cases, we have tested structural and electronic properties. Overall, the performance of the VPSIC approach can be summarized as follows: the predicted equilibrium structures are substantially in the same range of accuracy than those of the LDA and LSDA, with the VPSIC that on average reduces the bond lengths predicted by LDA and LSDA. This results to an average underestimate of the experimental lattice constant by about 1% for bulk systems and by just less than 2% for the molecule bond lengths. It is possible that the same approach built on top of the GGA might cure this problem since GGA generally overestimates bond lengths, and the SI removal would bring the final result closer to experiment. In contrast, as for the case of the PSIC and ASIC methods, the electronic properties are highly improved with respect to LDA and GGA, with bulk band gaps and molecular ionization potentials and electron affinities typically within 10% from the respective experimental determinations. The overall high quality of these results encourages us to pursue further explorations and applications of the VPSIC approach for finite and extended systems alike.

APPENDIX A: GENERALIZATION OF VPSIC FORMALISM TO USPP IMPLEMENTATION

For large-sized magnetic and strong-correlated systems, the ultrasoft pseudopotential (USPP) method[15] associated to a

plane-wave basis set is a formidable tool enabling the use of cutoff energies as low as 30–40 Ryd even for "hard" transition-metal ions such as Mn or Cu. The trade-off for this computational efficiency is a significant complication of the VPSIC formulas presented in Sec. II. In the following, we provide the VPSIC formulation adapted to the USPP formalism, which is our implementation of choice. For the sake of brevity, here we focus on the additional parts specific for the VPSIC approach, and refer the reader to Ref. 15 for details of the USPP formalism.

In short, in the USPP approach, the atomic valence charge is partitioned into outer ultrasoft (US) and intracore, augmented (AU) contributions. Only the former changes self-consistently with the surrounding chemical environment. Thus, the charge associated to the Bloch states $\psi_{n\mathbf{k}}^\sigma$ appearing in Sec. II only represents the very smooth US part. The Bloch states obey the generalized orthonormality conditions

$$\langle\,\psi_{n\mathbf{k}}^\sigma\,|\,\hat{S}\,|\,\psi_{n'\mathbf{k}}^\sigma\,\rangle \;=\; \delta_{n,n'}, \qquad (A1)$$

where the overall matrix $\hat{S}$ is given by

$$\hat{S} \;=\; \hat{I} + \sum_{ab,v} |\beta_{a,v}\rangle q_{ab,v}\langle\beta_{b,v}|. \qquad (A2)$$

Here, $\beta_{a,v}(\mathbf{r})$ and q_{abv} are, respectively, the atomic projector functions and the augmented charges characteristic of the USPP formalism, and (a,b) label atomic quantum numbers (l_a,m_a) ($q_{ab\mu}\neq 0$ only for $l_a = l_b$). Consistently, the total charge density is generalized as

$$n(\mathbf{r}) \;=\; \sum_{n\mathbf{k}\sigma}\langle\,\psi_{n\mathbf{k}}^\sigma\,|\,\hat{S}(\mathbf{r})\,|\,\psi_{n\mathbf{k}}^\sigma\,\rangle, \qquad (A3)$$

$$\hat{S}(\mathbf{r}) \;=\; |\mathbf{r}\rangle\langle\mathbf{r}| + \sum_{ab,v}|\beta_{a,v}\rangle Q_{abv}(\mathbf{r})\langle\beta_{b,v}|, \qquad (A4)$$

where $Q_{abv}(\mathbf{r})$ are augmented atomic charge densities. Within this generalized framework, the VPSIC energy functional described in Eq. (1) only includes the ultrasoft (US-SIC) part. In order to recover the full VPSIC energy functional, a further augmented contribution must be added:

$$E^{\text{VPSIC-AU}} \;=\; -\frac{1}{2}\sum_{ab\sigma v} B_{ab,v}^\sigma\, P_{ba,v}^\sigma\,\mathcal{E}_{ba,v}^{\text{AU}}, \qquad (A5)$$

where $B_{ab,v}^\sigma$ is the matrix of Bloch state projections onto the β-function basis

$$B_{ab,v}^\sigma \;=\; \sum_{n\mathbf{k}} f_{n\mathbf{k}}^\sigma\langle\,\psi_{n\mathbf{k}}^\sigma|\beta_{av}\rangle\langle\,\beta_{bv}|\psi_{n\mathbf{k}}^\sigma\rangle, \qquad (A6)$$

and $\mathcal{E}^{\text{AU}}$ are the SI energy associated to the augmented atomic charges $Q_{ab,v}(\mathbf{r})$:

$$\mathcal{E}_{ab,v}^{\text{AU}} \;=\; \int d\mathbf{r}\, Q_{ab,v}(\mathbf{r})\, V_{\text{Hxc}}[n_{av}(\mathbf{r}),0]. \qquad (A7)$$

In radial symmetry, $V_{\text{Hxc}}[n_{av},0] = V_{\text{Hxc}}[n_{bv},0]$ for $m_a \neq m_b$. Notice that we use different indices for the USPP projector (a, b) and for the SI projector (i, j) since the two basis sets are conceptually and practically different. The latter is built on a minimal set of atomic orbitals and, to be physically sound, it must be associated to bound atomic states. In contrast, in order to improve the USPP transferability, it is customary to

include in the (a,b) matrix more than one state per angular moment (typically, the bound atomic state plus one unbound state relative to some diagnostic energy reference). This difference introduces some ambiguities in Eq. (A7) relative to the definition of $V_{\text{Hxc}}[n_{av},0]$ and P_{abv}. The ambiguity can be solved by associating the same atomic V_{Hxc} (relative to the bound state) to all the beta projectors with same angular momentum l_a. Another possibility is that of rewriting the VPSIC-AU energy as

$$E^{\text{VPSIC-AU}}[\{\psi\}] \;=\; -\frac{1}{2}\sum_{ijv\sigma} P_{ijv}^\sigma\, P_{jiv}^\sigma\,\epsilon_{iv}^{\text{AU}}, \qquad (A8)$$

where

$$\epsilon_{iv}^{\text{AU}} \;=\; \sum_{ab}\langle\,\phi_{iv}\,|\,\beta_{av}\,\rangle\,\mathcal{E}_{ab,v}^{\text{AU}}\,\langle\,\beta_{bv}\,|\,\phi_{iv}\,\rangle \qquad (A9)$$

is just the augmented-only SI energy relative to the atomic state i at full occupancy and can be directly calculated in the atom. The use of the simplified Eq. (A8) bypasses altogether the explicit presence of the augmented charges, thus, greatly simplifying the VPSIC AU energy functional calculation. Since our many test cases reveal that Eqs. (A5) and (A8) give indeed very similar results, we decide to adopt the latter as standard choice. Then, Eq. (A8) brings a corresponding contribution to the VPSIC KS equations

$$\frac{\partial E^{\text{VPSIC-AU}}}{\partial\psi_{n\mathbf{k}\sigma}^*} \;=\; -\sum_{ijv} P_{ijv}^\sigma\,\frac{\partial P_{jiv}^\sigma}{\partial\psi_{n\mathbf{k}\sigma}^*}\epsilon_{jv}^{\text{AU}}. \qquad (A10)$$

Finally, the orbital occupations defined in Eq. (2) must be also generalized as

$$P_{ijv}^\sigma \;=\; \sum_{n\mathbf{k}} f_{n\mathbf{k}}^\sigma\langle\,\psi_{n\mathbf{k}}^\sigma|\tilde{\phi}_{iv}\rangle\,\langle\,\tilde{\phi}_{jv}|\psi_{n\mathbf{k}}^\sigma\rangle, \qquad (A11)$$

where the ultrasoft atomic orbitals ϕ_{iv} have been replaced by

$$|\tilde{\phi}_{iv}\rangle \;=\; \sum_{i'v'} S_{i'v',iv}^{-1/2}|\hat{S}\phi_{i'v'}\rangle, \qquad (A12)$$

with $\hat{S}$ given in Eq. (A2). Thus, we have

$$|\hat{S}\phi_{iv}\rangle \;=\; |\phi_{iv}\rangle + \sum_{ab,\mu}|\beta_{a\mu}\rangle q_{ab,\mu}\langle\beta_{b\mu}|\phi_{iv}\rangle, \qquad (A13)$$

and

$$S_{iv,i'v'} \;=\; \langle\,\phi_{iv}\,|\,\hat{S}\,|\,\phi_{i'v'}\,\rangle \qquad (A14)$$

is the overlap matrix in the atomic-orbital basis set. By construction, this is Hermitian and also positive defined, so its square-root matrix can always be defined in the following, unique way: Since (dropping indexes for clarity) $[\hat{S}^{-1/2},\hat{S}] = 0$, $\hat{S}$ can be diagonalized in the (i,j) subspace, and from its eigenvalues λ_k, we have $S_{kk'}^{-1/2} = \delta_{kk'}\,\lambda_k^{-1/2}$. The latter is finally rotated back to the original (i,j) basis set to obtain $S_{ij}^{-1/2}$.

The replacement of simple atomic-site-centered ϕ_{iv} orbitals with the $\tilde{\phi}_i$ orbitals given by Eq. (A12) (known as[81] Löwdin orthonormalization) is required by the necessity to enforce, at any $\{\mathbf{R}\}$, the orthonormality conditions $\langle\tilde{\phi}_{iv}|\tilde{\phi}_{jv'}\rangle = \delta_{ij}\delta_{vv'}$ and, in turn, the correct normalization of the orbital occupation matrix defined in Eq. (A11). Upon diagonalization, $0 \leqslant P_{iiv}^\sigma \leqslant 1$ and $\sum_{iv\sigma} P_{iiv}^\sigma = N$, with N the total number of electrons in

the cell. These constraints are essential to the interpretation of P_{iiv}^{σ} as physically sound orbital occupancy.

In contrast, the Löwdin renormalization implies a remarkable complication in the formulation of the atomic forces since it is clear from Eqs. (A12) and (A14) that $\tilde{\phi}_{iv}$ is not simply centered on a single atomic site, but includes contributions from the overlap with all other atomic orbitals $\phi_{j\mu}$ as well as beta functions $\beta_{a\mu}$ of the cell. Since the forces formulation in the case of Löwdin-normalized orbitals may be useful even in other methodological contexts (e.g., in the LDA + U method, the Hamiltonian of which is also written in terms of orbital occupancies), we dedicate the next section to describe it in detail.

APPENDIX B: FORCES FORMULATION WITHIN PLANE WAVES AND USPP

In the case of USPP formalism, the forces expression given in Eq. (19) [or Eq. (20) if the simplified approach is considered] must be generalized in order to include the contribution generated by the additional AU energy of Eq. (A8):

$$-\frac{\partial E^{\mathrm{AU}}[\{\psi\}]}{\partial \mathbf{R}_\nu}$$
$$= \sum_{ij,nk\sigma} f_{n\mathbf{k}}^{\sigma} \left\{ P_{ij\nu}^{\sigma} \epsilon_{j\nu}^{\mathrm{AU}} \left\langle \psi_{n\mathbf{k}}^{\sigma} \left| \frac{\partial \phi_{j,\nu}}{\partial \mathbf{R}_\nu} \right. \right\rangle \langle \phi_{i,\nu} | \psi_{n\mathbf{k}}^{\sigma} \rangle + \mathrm{c.c.} \right\}. \tag{B1}$$

When using a plane-wave basis set, the implementation of Eqs. (19), (20), or (B1) is rather straightforward except for one ingredient, which requires attention: the atomic-orbital derivative. The simplest case is that of atomic orbitals that remain centered on the atomic positions (i.e., orbitals that simply translate along with their reference atom displacement). In this case, the force on a given atom $\mathbf{R}_\nu$ only depends on the change of the orbitals sited on ν, and the orbital derivative is easily calculated as

$$\frac{\partial}{\partial \mathbf{R}_\nu} \langle \mathbf{k} + \mathbf{G} | \phi_{iv} \rangle = \frac{\partial}{\partial \mathbf{R}_\nu} e^{-i(\mathbf{k}+\mathbf{G})\cdot \mathbf{R}_\nu} \langle \mathbf{k} + \mathbf{G} | \phi_{i0} \rangle$$
$$= -i(\mathbf{k} + \mathbf{G}) \langle \mathbf{k} + \mathbf{G} | \phi_{iv} \rangle, \tag{B2}$$

where, clearly, $\phi_{iv} = \phi_{iv}(\mathbf{r} - \mathbf{R}_\nu)$ and $\phi_{i0} = \phi_i(\mathbf{r})$. However, as discussed in the previous section, orbitals ϕ_{iv} must be replaced by $\tilde{\phi}_{iv}$, and the forces equation generalized accordingly to

$$-\frac{\partial E^{\mathrm{VPSIC}}[\{\psi\}]}{\partial \mathbf{R}_\nu} = \mathbf{F}_\nu^{\mathrm{LSD}}$$
$$+ \frac{1}{2} \sum_{ij,nk\sigma} f_{n\mathbf{k}}^{\sigma} \left\{ \left\langle \psi_{n\mathbf{k}}^{\sigma} \left| \frac{\partial \gamma_{i,\nu}}{\partial \mathbf{R}_\nu} \right. \right\rangle C_{ij} \langle \gamma_{j,\nu} | \psi_{n\mathbf{k}}^{\sigma} \rangle P_{ji\nu}^{\sigma} + \mathrm{c.c.} \right\}$$
$$+ \frac{1}{2} \sum_{ij\mu,nk\sigma} f_{n\mathbf{k}}^{\sigma} \left\{ \mathcal{E}_{ij\sigma\mu}^{\mathrm{SI}} \left\langle \psi_{n\mathbf{k}}^{\sigma} \left| \frac{\partial \tilde{\phi}_{i,\mu}}{\partial \mathbf{R}_\nu} \right. \right\rangle \langle \tilde{\phi}_{j,\mu} | \psi_{n\mathbf{k}}^{\sigma} \rangle + \mathrm{c.c.} \right\}$$
$$+ \sum_{ij\mu nk\sigma} f_{n\mathbf{k}}^{\sigma} \left\{ P_{ij\mu}^{\sigma} \epsilon_{j\mu}^{\mathrm{AU}} \left\langle \psi_{n\mathbf{k}}^{\sigma} \left| \frac{\partial \tilde{\phi}_{j\mu}}{\partial \mathbf{R}_\nu} \right. \right\rangle \langle \tilde{\phi}_{i\mu} | \psi_{n\mathbf{k}}^{\sigma} \rangle + \mathrm{c.c.} \right\}. \tag{B3}$$

Here, the first two terms account for the US contribution and the third for the AU part. The presence of the

Löwdin-normalized orbitals brings one more sum over the atomic positions in the second and third terms since now the displacement of one single atom in $\mathbf{R}_\nu$ changes, in principle, all the orbitals, not just those sited on $\mathbf{R}_\nu$. The Löwdin orbital derivatives gives

$$\left\langle \psi_{n\mathbf{k}} \left| \frac{\partial \tilde{\phi}_{j\mu}}{\partial \mathbf{R}_\nu} \right. \right\rangle = S_{j'\mu',j\mu}^{-1/2} \left\langle \psi_{n\mathbf{k}} \left| \frac{\partial \hat{S}\phi_{j'\mu'}}{\partial \mathbf{R}_\nu} \right. \right\rangle$$
$$+ \frac{\partial S_{j'\mu',j\mu}^{-1/2}}{\partial \mathbf{R}_\nu} \langle \psi_{n\mathbf{k}} | \hat{S}\phi_{j'\mu'} \rangle \tag{B4}$$

(where sum over repeated indices is understood).

Let us start by considering the first term

$$\left\langle \psi_{n\mathbf{k}} \left| \frac{\partial \hat{S}\phi_{j'\mu'}}{\partial \mathbf{R}_\nu} \right. \right\rangle$$
$$= \left\langle \psi_{n\mathbf{k}} | \hat{S} \left| \frac{\partial \phi_{j'\mu'}}{\partial \mathbf{R}_\nu} \right. \right\rangle + \left\langle \psi_{n\mathbf{k}} \left| \frac{\partial \hat{S}}{\partial \mathbf{R}_\nu} \right| \phi_{j'\mu'} \right\rangle$$
$$= \left[\left\langle \psi_{n\mathbf{k}} \left| \frac{\partial \phi_{j'\mu'}}{\partial \mathbf{R}_\nu} \right. \right\rangle + \sum_{abv'} \langle \psi_{n\mathbf{k}} | \beta_{av'} \rangle q_{abv'} \left\langle \beta_{bv'} \left| \frac{\partial \phi_{j'\mu'}}{\partial \mathbf{R}_\nu} \right. \right\rangle \right] \delta_{\mu'\nu}$$
$$+ \sum_{abv'} \left[\left\langle \psi_{n\mathbf{k}} \left| \frac{\partial \beta_{av'}}{\partial \mathbf{R}_\nu} \right. \right\rangle q_{abv'} \langle \beta_{bv'} | \phi_{j'\mu'} \rangle \right.$$
$$\left. + \langle \psi_{n\mathbf{k}} | \beta_{av'} \rangle q_{abv'} \left\langle \frac{\partial \beta_{bv'}}{\partial \mathbf{R}_\nu} \right| \phi_{j'\mu'} \right\rangle \right] \delta_{\nu'\nu}. \tag{B5}$$

Here, the first term in square brackets selects the contribution to the derivative due to the atomic orbital $\phi_{j'\mu'}$ displacement, while the second term selects the contribution due to the β-functions displacement. Despite the apparent complexity, Eq. (B5) is rather straightforward to calculate in plane waves since all these derivatives are easily obtained through Eq. (B2).

The calculation of the second term in Eq. (B5), which includes an uncommon square-root-matrix derivative, is more involved. We can proceed as follows (dropping the atomic indices for brevity): from $S^{-1/2} S^{-1/2} = S^{-1}$, we obtain

$$\frac{\partial S^{-1}}{\partial \mathbf{R}} = \frac{\partial S^{-1/2}}{\partial \mathbf{R}} S^{-1/2} + S^{-1/2} \frac{\partial S^{-1/2}}{\partial \mathbf{R}}. \tag{B6}$$

The left-hand side of Eq. (B6) can be transformed by using the expression

$$\frac{\partial S^{-1}}{\partial \mathbf{R}} = S^{-1} \frac{\partial S}{\partial \mathbf{R}} S^{-1}, \tag{B7}$$

where S^{-1} can be easily obtained from S (just like $S^{-1/2}$, as explained in the previous section). Then, we need to calculate the overlap matrix derivative (reintroducing atomic indices) as

$$\frac{\partial S_{i\mu,i'\mu'}}{\partial \mathbf{R}_\nu} = \left\langle \frac{\partial \phi_{i\mu}}{\partial \mathbf{R}_\nu} \left| \hat{S} \right| \phi_{i'\mu'} \right\rangle$$
$$+ \left\langle \phi_{i\mu} \left| \hat{S} \right| \frac{\partial \phi_{i'\mu'}}{\partial \mathbf{R}_\nu} \right\rangle + \left\langle \phi_{i\mu} \left| \frac{\partial \hat{S}}{\partial \mathbf{R}_\nu} \right| \phi_{i'\mu'} \right\rangle. \tag{B8}$$

This expression is clearly similar to that in Eq. (B5) and we can give it as understood. Therefore, the matrix on the left-hand side in Eq. (B6) is determined. Now, by looking at the right

side, we notice that, if $S^{-1/2}$ commutes with its derivative, the latter is easily extracted as

$$\frac{\partial S^{-1/2}}{\partial \mathbf{R}} = \frac{1}{2}\frac{\partial S^{-1}}{\partial \mathbf{R}} S^{-1/2}. \qquad (B9)$$

However, they do not generally commute (except when the Hermitian matrix $S^{-1/2}$ is also real) and Eq. (B9) does not hold. Thus, we need to solve Eq. (B6), which is nothing but a Lyapunov matrix equation of the form $B = XA + AX$, where the known terms are $A = S^{-1/2}$ and $B = dS^{-1}/dR$, and $X = dS^{-1/2}/dR$. The general Lyapunov equation can be solved exactly, but for the specific values of A and B, we can apply the simple strategy proposed in Ref. 80, which we repeat here to the benefit of the reader: we can rewrite $A = CVC^+$, where V and C can be easily determined as the diagonalized matrix and the basis change matrix; then, we can multiply both members of Eq. (B6) by C^+ on the left-hand side and C on the right-hand side:

$$C^+BC = C^+AXC + C^+XAC = VC^+XC + C^+XCV. \qquad (B10)$$

By introducing $R = C^+BC$ and $Y = C^+XC$, Eq. (B10) can be rewritten as $R = VY + YV$, which is now trivially solved, given the diagonal character of V:

$$Y_{ij} = \frac{R_{ij}}{V_{ii} + V_{jj}}. \qquad (B11)$$

Once Y is determined, the unknown X can be finally obtained as $X = CYC^+$.

APPENDIX C: VPSIC FORMALISM WITHIN ATOMIC-ORBITALS BASIS SET

As the VPSIC correction is based on a projection of the occupied KS orbital manifold onto a localized subspace of atomic orbitals, the formalism naturally lends itself to an implementation within a localized orbital basis set framework. Here, we provide some details of the current VPSIC implementation within the SIESTA code.[6] The first step in setting up the VPSIC algorithm consists in constructing a minimal set of atomic orbitals $\{\phi_{i,\nu}\}$ and the associated projectors $\{\gamma_{i,\nu}\}$, which will be used to calculate the occupation numbers [Eq. (2)] and the effective SI energies [Eq. (3)]. Within SIESTA, the functions $\phi_{i,\nu}$ are numerical pseudoatomic orbitals with a finite range, constructed as solutions of the atomic Schrödinger equation with an additional confining potential at the cutoff radius r_c.[6] The finite extent of the functions $\phi_{i,\nu}$ ensures that the corresponding SIC projectors $\gamma_{i,\nu}$ [Eq. (4)] also vanish beyond r_c. In the current implementation, the SIC potential $V_{\text{Hxc}}[\rho_{\nu,l_i}(r);1]$ in Eq. (4) is obtained from a full PZ-SIC-LSDA (Ref. 7) calculation for a free atom and imported into SIESTA via a pseudopotential. An appropriate choice for the cutoff radius r_c is then dictated by the requirement that the expectation value

$$\delta\varepsilon_{i,\nu}^{\text{SIC}} = \int d\mathbf{r}\, \phi_{l_i,m_i}(\mathbf{r})\, V_{\text{Hxc}}[\rho_{\nu,l_i}(r);1]\, \phi_{l_i,m_i}(\mathbf{r}) \qquad (C1)$$

reproduces the PZ-SIC-LSDA correction of the corresponding orbital in the free atom to within a small tolerance. Simultaneously, the cutoff should be reasonably short so as not to change

the connectivity of the matrix elements of the pseudoatomic orbital (PAO) Hamiltonian. Therefore, in practice, we set the cutoff radius for the projection orbitals on a given atom $\phi_{i,\nu}$ to be either equal to the largest among the cutoff radii of the PAO basis set for that particular atom (typically, the first ζ of the lowest angular momentum) or, if shorter, to the radius at which $\delta\varepsilon_{i,\nu}^{\text{SIC}} < 0.1$ mRy. For typical cutoff radii (6 to 9 Bohr), we find that the atomic SIC-LSDA eigenvalues are reproduced to within 1 to 5 mRy for the most extended shells and to within 0.1 mRy for more confined ones. Thus, $\delta\varepsilon_{i,\nu}^{\text{SIC}}$ is rather well converged already for cutoff radii defined by PAO energy shifts[6] of around 20 mRy.

By using the orbitals $\phi_{i,\nu}$ and the projectors $\{\gamma_{i,\nu}\}$, the occupation numbers $p_{ij\nu}^{\sigma}$ and the effective SI energies $\epsilon_{ij\sigma\nu}^{\text{SI}}$ for the extended system can be calculated. Different choices are possible for the projection operators that yield the occupation numbers $p_{ij\nu}^{\sigma}$. In our implementation, we use the so-called *dual* projection operator given by

$$\hat{P}_{ij\nu}^{\sigma} = \frac{1}{2}\{|\widetilde{\phi_{i,\nu}}\rangle\langle\phi_{j,\nu}| + |\phi_{i,\nu}\rangle\langle\widetilde{\phi_{j,\nu}}|\}, \qquad (C2)$$

where $|\widetilde{\phi_{i,\nu}}\rangle$ is the dual orbital of $|\phi_{i,\nu}\rangle$ and is given by

$$|\widetilde{\phi_{i,\nu}}\rangle = \sum_{j,\mu} S_{i\nu,j\mu}^{-1}|\phi_{j,\mu}\rangle, \qquad (C3)$$

with S^{-1} being the inverse of the overlap matrix over the nonorthogonal set $\{\phi_{i,\nu}\}$:

$$S_{i\nu,j\mu} = \langle\phi_{i,\nu}|\phi_{j,\mu}\rangle. \qquad (C4)$$

The dual orbitals satisfy the orthogonality relation

$$\langle\widetilde{\phi_{i,\nu}}|\phi_{j,\mu}\rangle = \delta_{i\nu,j\mu}. \qquad (C5)$$

With this choice for the occupation number operator, the matrix elements of the VPSIC potential between two basis functions α, β become

$$V_{\alpha\beta\sigma}^{\text{SIC}} = \frac{1}{2}\sum_{ij\nu}\epsilon_{ij\sigma\nu}^{\text{SI}}\left\{\frac{1}{2}[\langle\alpha|\widetilde{\phi_{i,\nu}}\rangle\langle\phi_{j,\nu}|\beta\rangle \right.$$
$$\left. + \langle\alpha|\phi_{i,\nu}\rangle\langle\widetilde{\phi_{j,\nu}}|\beta\rangle]\right\} + p_{ij\nu}^{\sigma}\langle\alpha|\gamma_{i,\nu}\rangle C_{ij\nu}\langle\gamma_{j,\nu}|\beta\rangle. \qquad (C6)$$

The expression for the VPSIC contribution to the atomic forces also involves two-center-type integrals and their derivatives. By setting $\Omega_{\alpha,i\nu} = \langle\alpha|\phi_{i,\nu}\rangle$, $\tilde{\Omega}_{\alpha,i\nu} = \langle\alpha|\widetilde{\phi_{i,\nu}}\rangle$, and $G_{\alpha,i\nu} = \langle\alpha|\gamma_{i,\nu}\rangle$, we have

$$\mathbf{F}_{\mu}^{\text{SIC}} = -\frac{\partial E^{\text{SIC}}[\{\psi\}]}{\partial \mathbf{R}_{\mu}}$$
$$= \frac{1}{2}\sum_{ij\nu\sigma}\epsilon_{ij\nu\sigma}^{\text{SI}}\frac{\partial p_{ij\nu}^{\sigma}}{\partial \mathbf{R}_{\mu}} + p_{ij\nu}^{\sigma}\frac{\partial\epsilon_{ij\nu\sigma}^{\text{SI}}}{\partial \mathbf{R}_{\mu}}, \qquad (C7)$$

with

$$\frac{\partial p_{ij\nu}^{\sigma}}{\partial \mathbf{R}_{\mu}} = \frac{1}{2}\sum_{\alpha\beta}\frac{\partial\rho_{\beta\alpha}^{\sigma}}{\partial \mathbf{R}_{\mu}}[\tilde{\Omega}_{\alpha,i\nu}\Omega_{\beta,j\nu} + \Omega_{\alpha,i\nu}\tilde{\Omega}_{\beta,j\nu}]$$
$$+ \rho_{\beta\alpha}^{\sigma}\left[\frac{\partial\tilde{\Omega}_{\alpha,i\nu}}{\partial \mathbf{R}_{\mu}}\Omega_{\beta,j\nu} + \tilde{\Omega}_{\alpha,i\nu}\frac{\partial\Omega_{\beta,j\nu}}{\partial \mathbf{R}_{\mu}}\right.$$
$$\left. + \frac{\partial\Omega_{\alpha,i\nu}}{\partial \mathbf{R}_{\mu}}\tilde{\Omega}_{\beta,j\nu} + \Omega_{\alpha,i\nu}\frac{\partial\tilde{\Omega}_{\beta,j\nu}}{\partial \mathbf{R}_{\mu}}\right] \qquad (C8)$$

and

$$\frac{\partial \epsilon_{ij\nu\sigma}^{SI}}{\partial \mathbf{R}_\mu} = \sum_{\alpha\beta} \frac{\partial \rho_{\beta\alpha}^\sigma}{\partial \mathbf{R}_\mu} G_{\alpha,i\nu} C_{ij\nu} G_{\beta,j\nu}$$
$$+ \rho_{\beta\alpha}^\sigma \left[\frac{\partial G_{\alpha,i\nu}}{\partial \mathbf{R}_\mu} C_{ij\nu} G_{\beta,j\nu} + G_{\alpha,i\nu} C_{ij\nu} \frac{\partial G_{\beta,j\nu}}{\partial \mathbf{R}_\mu} \right],$$
(C9)

where the sum is over the SIESTA basis functions α, β, and $\rho_{\beta\alpha}^\sigma$ is the density matrix given by

$$\rho_{\beta\alpha}^\sigma = \sum_{n\mathbf{k}} f_{n\mathbf{k}}^\sigma \langle \beta | \psi_{n\mathbf{k}}^\sigma \rangle \langle \psi_{n\mathbf{k}}^\sigma | \alpha \rangle.$$
(C10)

Quantities of the type $\frac{\partial \Omega_{\alpha,i\nu}}{\partial \mathbf{R}_\mu}$ and $\frac{\partial G_{\alpha,i\nu}}{\partial \mathbf{R}_\mu}$ are easily calculated as derivatives of two-center integrals as they vanish unless one of the functions $|\alpha\rangle$ or $|\phi_{i,\nu}\rangle$ is centered on the atom at $\mathbf{R}_\mu$. However, the dual orbitals $|\widetilde{\phi_{i,\nu}}\rangle$ are not simple atom-centered functions, and derivatives of the type $\frac{\partial \tilde{\Omega}_{\alpha,i\nu}}{\partial \mathbf{R}_\mu}$ can be nonzero even when neither $|\alpha\rangle$ nor $|\phi_{i,\nu}\rangle$ is centered on atom μ. These may, in principle, be evaluated as follows. We start by expanding the matrix element between a SIESTA basis function $|\alpha\rangle$ and a projector function $|\phi_{i,\nu}\rangle$ by inserting the identity operator in the space of projector functions

$$\langle \alpha | \phi_{i,\nu} \rangle = \sum_{\mu,j} \langle \alpha | \widetilde{\phi_{j,\mu}} \rangle \langle \phi_{j,\mu} | \phi_{i,\nu} \rangle.$$
(C11)

The derivative of this expression with respect to $\mathbf{R}_I$ where I is any atom index is

$$\frac{\partial}{\partial \mathbf{R}_I} \langle \alpha | \phi_{i,\nu} \rangle = \sum_{\mu,j} \frac{\partial \langle \alpha | \widetilde{\phi_{j,\mu}} \rangle}{\partial \mathbf{R}_I} \langle \phi_{j,\mu} | \phi_{i,\nu} \rangle$$
$$+ \langle \alpha | \widetilde{\phi_{j,\mu}} \rangle \frac{\partial \langle \phi_{j,\mu} | \phi_{i,\nu} \rangle}{\partial \mathbf{R}_I}.$$
(C12)

A similar equation can be written for all of the matrix elements in the overlap matrix Ω of basis functions with projector functions $\Omega_{\alpha,i\nu} = \langle \alpha | \phi_{i,\nu} \rangle$ so that the above equation is equivalent to the matrix equation

$$\nabla_{\mathbf{R}_I} \Omega = (\nabla_{\mathbf{R}_I} \tilde{\Omega}) \cdot S + \tilde{\Omega} \cdot (\nabla_{\mathbf{R}_I} S),$$
(C13)

where in $\tilde{\Omega}_{\alpha,j\mu} = \langle \alpha | \widetilde{\phi_{j,\mu}} \rangle$ and S is the overlap matrix in the space of the projector functions as defined in Eq. (C4). The required derivatives involving the dual orbitals $\frac{\partial \langle \alpha | \widetilde{\phi_{j,\mu}} \rangle}{\partial \mathbf{R}_I}$ in Eq. (C12) are the elements of $\nabla_{\mathbf{R}_I} \tilde{\Omega}$, which can be solved for as

$$\nabla_{\mathbf{R}_I} \tilde{U} = \left[\nabla_{\mathbf{R}_I} U - \tilde{U} \cdot (\nabla_{\mathbf{R}_I} S) \right] \cdot S^{-1}.$$
(C14)

A corresponding set of equations can be written down involving the derivatives of the matrix elements $W_{i\nu,\alpha} = \langle \phi_{i,\nu} | \alpha \rangle$ and $\tilde{W}_{i\nu,\alpha} = \langle \widetilde{\phi_{i,\nu}} | \alpha \rangle$ with $\nabla_{\mathbf{R}_I} \tilde{W}$ being given by

$$\nabla_{\mathbf{R}_I} \tilde{W} = S^{-1} \cdot \left[\nabla_{\mathbf{R}_I} W - (\nabla_{\mathbf{R}_I} S) \cdot \tilde{W} \right].$$
(C15)

Equations (C14) and (C15) can be readily evaluated as all the derivatives appearing on the right-hand side are simple two-center integrals and, furthermore, S^{-1} is well defined since S is a square matrix and positive definite. However, this additional linear algebra required to handle the dual orbitals $|\widetilde{\phi_{i,\nu}}\rangle$ is rather cumbersome as Eqs. (C14) and (C15) need to be solved

separately for each atom in the system. In order to avoid these additional computational overheads in estimating the forces, one may in practice adopt a slightly different approach for calculating the VPSIC orbital occupation numbers within the framework of a localized orbital basis. This is described in Appendix D.

APPENDIX D: SIMPLIFIED VPSIC ORBITAL OCCUPATION SCHEME FOR LCAO BASIS SETS

We take advantage of the Mülliken orbital population decomposition of the electronic charge density readily available in SIESTA[6] and define the VPSIC occupation number $p_{ij\nu}^\sigma$ as a sum over the Mülliken occupations of the underlying local orbital basis set. Since SIESTA employs a multiple-ζ numerical basis set,[6] it is possible to define a mapping between a VPSIC projector on an atom and basis orbitals on the same atom enumerated by their ζ index. For instance, on any atom, a VPSIC projector function $|\phi_{i,\nu}\rangle$, with the index i specifying cumulatively the (n, l, m) quantum numbers, can be mapped to all of the basis functions on the atom with the same (n, l, m) quantum numbers, but with different ζ indices. Thus, in the case of a single-ζ basis being employed, there is a one-to-one correspondence between the VPSIC projector functions and the orbitals in the basis set. Within this scheme, polarization orbitals in the basis set are treated simply as additional ζ functions of higher-l quantum number. Therefore, all basis functions corresponding to a given projector function $|\phi_{i,\nu}\rangle$ may be represented by attaching an additional multiplicity index ζ as $|\varphi_{i\zeta\nu}\rangle$. The VPSIC occupation numbers are then given by

$$p_{ij\nu}^\sigma = \sum_\zeta p_{ij,\zeta,\nu}^\sigma = \frac{1}{2} \sum_\alpha \sum_\zeta \left(\rho_{i\zeta\nu,\alpha}^\sigma S_{\alpha,j\zeta\nu} + S_{i\zeta\nu,\alpha} \rho_{\alpha,j\zeta\nu}^\sigma \right),$$
(D1)

where $p_{ij,\zeta,\nu}^\sigma$ is the overlap occupation number for the pair of basis functions $|\varphi_{i\zeta\nu}\rangle$ and $|\varphi_{j\zeta\nu}\rangle$. The sum over the index α represents an unrestricted summation over all of the basis functions in the calculation. The terms $\rho_{i\zeta\nu,\alpha}^\sigma$ and $S_{i\zeta\nu,\alpha}$ are, respectively, the spin density matrix and the overlap matrix elements between basis functions $|\varphi_{i\zeta\nu}\rangle$ and $|\alpha\rangle$. By defining the VPSIC occupation numbers in this way, we avoid having to deal with the dual orbitals [see Eq. (C3)] of the projector functions. Furthermore, the occupation numbers defined in Eq. (D1) satisfy the sum rule

$$\sum_{i\nu,\sigma} p_{ii\nu}^\sigma = N,$$
(D2)

i.e., the diagonal occupations $p_{ii\nu}^\sigma$ sum to the total number of electrons N in the system. The VPSIC forces follow once again from Eq. (C7), but with

$$\frac{\partial p_{ij\nu}^\sigma}{\partial \mathbf{R}_\mu} = \frac{1}{2} \sum_{\alpha\zeta} \left\{ \frac{\partial \rho_{i\zeta\nu,\alpha}^\sigma}{\partial \mathbf{R}_\mu} S_{\alpha,j\zeta\nu} + \rho_{i\zeta\nu,\alpha}^\sigma \frac{\partial S_{\alpha,j\zeta\nu}}{\partial \mathbf{R}_\mu} \right.$$
$$\left. + \frac{\partial S_{i\zeta\nu,\alpha}}{\partial \mathbf{R}_\mu} \rho_{\alpha,j\zeta\nu}^\sigma + S_{i\zeta\nu,\alpha} \frac{\partial \rho_{\alpha,j\zeta\nu}^\sigma}{\partial \mathbf{R}_\mu} \right\}.$$
(D3)

The terms such as $\frac{\partial \rho_{i\zeta\nu,\alpha}^\sigma}{\partial \mathbf{R}_\mu}$, involving the derivatives of the density matrix, are treated separately, being incorporated into

the orthogonality force and stress contributions.[6] In contrast, the derivatives of the overlap matrix with respect to atomic positions $\frac{\partial S_{i\xi\nu,\alpha}}{\partial \mathbf{R}_\mu}$ are readily available in Ref. 6. We note that

results obtained by adopting Eq. (D1) to define the occupation numbers are very similar to those obtained by using the original definition of Eq. (2).

[1] A. Ohtomo and H. Y. Hwang, Nature (London) **427**, 423 (2004).

[2] V. I. Anisimov, J. Zaanen, and O. K. Andersen, Phys. Rev. B **44**, 943 (1991).

[3] A. Filippetti and N. A. Spaldin, Phys. Rev. B **67**, 125109 (2003).

[4] A. Filippetti and V. Fiorentini, Eur. Phys. J. B **71**, 139 (2009).

[5] C. D. Pemmaraju, T. Archer, D. Sanchez-Portal, and S. Sanvito, Phys. Rev. B **75**, 045101 (2007).

[6] J. M. Soler, E. Artacho, J. D. Gale, A. García, J. Junquera, P. Ordejón, and D. Sanchez-Portal, J. Phys.: Condens. Matter **14**, 2745 (2002).

[7] J. P. Perdew and A. Zunger, Phys. Rev. B **23**, 5048 (1981).

[8] A. Svane and O. Gunnarsson, Phys. Rev. Lett. **65**, 1148 (1990).

[9] Z. Szotek et al., Phys. B (Amsterdam) **172**, 19 (1991).

[10] M. Stengel and N. A. Spaldin, Phys. Rev. B **77**, 155106 (2008).

[11] C. D. Pemmaraju, I. Rungger, X. Chen, A. R. Rocha, and S. Sanvito, Phys. Rev. B **82**, 125426 (2010).

[12] T. Archer, C. D. Pemmaraju, S. Sanvito, C. Franchini, J. He, A. Filippetti, P. Delugas, D. Puggioni, and V. Fiorentini, Phys. Rev. B **84**, 115114 (2011).

[13] P. Delugas, A. Filippetti, V. Fiorentini, D. I. Bilc, D. Fontaine, and Ph. Ghosez, Phys. Rev. Lett. **106**, 166807 (2011).

[14] L. Kleinman and D. M. Bylander, Phys. Rev. Lett. **48**, 1425 (1982).

[15] D. Vanderbilt, Phys. Rev. B **41**, R7892 (1990).

[16] D. C. Cronemeyer, Phys. Rev. **87**, 876 (1952).

[17] P. Moch, M. Balkanski, and P. Aigrain, C. R. Acad. Sci. (Paris) **251**, 1373 (1960).

[18] J. Riga, C. Tenret-Noël, J. J. Pireaux, R. Caudano, J. J. Verbist, and Y. Gobillon, Phys. Scr. **16**, 351 (1977).

[19] K. van Benthem, C. Elsässer, and R. H. French, J. Appl. Phys. **90**, 6156 (2001).

[20] Extrapolated from photoemission spectra reported in K. Yoshimatsu, R. Yasuhara, H. Kumigashira, and M. Oshima, Phys. Rev. Lett **101**, 026802 (2008).

[21] T. V. Perevalov and V. A. Gritsenko, J. Exp. Theor. Phys. **112**, 310 (2011).

[22] I. A. Nekrasov, M. A. Korotin, and V. I. Anisimov, e-print arXiv:cond-mat/0009107.

[23] G. Cappellini, S. Bouette-Russo, B. Amadon, C. Noguera, and F. Finocchi, J. Phys.: Condens. Matter **12**, 3671 (2000).

[24] G. Khaliullin and S. Okamoto, Phys. Rev. Lett. **89**, 167201 (2002).

[25] M. Tsubota, F. Iga, T. Takabatake, N. Kikugawa, T. Suzuki, I. Oguro, H. Kawanaka, and H. Bando, Phys. B (Amsterdam) **281-282**, 622 (2000).

[26] H. Nakao, Y. Wakabayashi, T. Kiyama, Y. Murakami, M. V. Zimmermann, J. P. Hill, D. Gibbs, S. Ishihara, Y. Taguchi, and Y. Tokura, Phys. Rev. B **66**, 184419 (2002).

[27] M. Mochizuki and M. Imada, Phys. Rev. Lett. **91**, 167203 (2003).

[28] M. Cwik, T. Lorenz, J. Baier, R. Müller, G. André, F. Bourée, F. Lichtenberg, A. Freimuth, R. Schmitz, E. Müller-Hartmann, and M. Braden, Phys. Rev. B **68**, 060401(R) (2003).

[29] B. Keimer, D. Casa, A. Ivanov, J. W. Lynn, M. V. Zimmermann, J. P. Hill, D. Gibbs, Y. Taguchi, and Y. Tokura, Phys. Rev. Lett. **85**, 3946 (2000).

[30] T. Kiyama and M. Itoh, Phys. Rev. Lett. **91**, 167202 (2003).

[31] G. Khaliullin and S. Maekawa, Phys. Rev. Lett. **85**, 3950 (2000).

[32] L. Craco, M. S. Laad, S. Leoni, and E. Müller-Hartmann, Phys. Rev. B **70**, 195116 (2004); L. Craco, S. Leoni, and E. Müller-Hartmann, *ibid.* **74**, 155128 (2006)

[33] M. W. Haverkort et al., Phys. Rev. Lett. **94**, 056401 (2005).

[34] J. Hemberger et al., Phys. Rev. Lett. **91**, 066403 (2003).

[35] P. Lunkenheimer, T. Rudolf, J. Hemberger, A. Pimenov, S. Tachos, F. Lichtenberg, and A. Loidl, Phys. Rev. B **68**, 245108 (2003).

[36] H. Fujitani and S. Asano, Phys. Rev. B **51**, 2098 (1995).

[37] H. Sawada and K. Terakura, Phys. Rev. B **58**, 6831 (1998).

[38] S. V. Streltsov, A. S. Mylnikova, A. O. Shorikov, Z. V. Pchelkina, D. I. Khomskii, and V. I. Anisimov, Phys. Rev. B **71**, 245114 (2005).

[39] E. Pavarini, S. Biermann, A. Poteryaev, A. I. Lichtenstein, A. Georges, and O. K. Andersen, Phys. Rev. Lett. **92**, 176403 (2004).

[40] I. V. Solovyev, Phys. Rev. B **74**, 054412 (2006).

[41] I. A. Nekrasov, K. Held, N. Blümer, A. I. Poteryaev, V. I. Anisimov, and D. Vollhardt, Eur. Phys. J. B **18**, 55 (2000).

[42] For a 45° rotation in the (x, y) plane, $|xy\rangle \rightarrow |x^2 - y^2\rangle$, $|xz\rangle \rightarrow (|xz\rangle + |yz\rangle)/\sqrt{2}$, $|yz\rangle \rightarrow (|yz\rangle - |xz\rangle)/\sqrt{2}$.

[43] F. Iga, M. Tsubota, M. Sawada, H. B. Huang, S. Kura, M. Takemura, K. Yaji, M. Nagira, A. Kimura, T. Jo, T. Takabatake, H. Namatame, and M. Taniguchi, Phys. Rev. Lett. **93**, 257207 (2004).

[44] Note that we use a different reference configuration than Ref. 43, which assumes a local cubic reference system where z changes according to Ti, so as to be always parallel to the longer Ti–O bond. See our structural analysis later on.

[45] J. B. Goodenough, J. Phys. Chem. Solids **6**, 287 (1958); J. Kanamori, *ibid.* **10**, 87 (1959); J. B. Goodenough, Scholarpedia **3**, 7382 (2008).

[46] W. E. Pickett and D. J. Singh, Phys. Rev. B **53**, 1146 (1996).

[47] S. Satpathy, Z. S. Popovic, and F. R. Vukajlovic, Phys. Rev. Lett. **76**, 960 (1996).

[48] C. Cardoso, R. P. Borges, T. Gasche, and M. Godinho, J. Phys.: Condens. Matter **20**, 035202 (2008).

[49] T. Saha-Dasgupta and S. Satpathy, J. Phys.: Condens. Matter **15**, 1685 (2003).

[50] A. Filippetti and N. A. Hill, Phys. Rev. B **65**, 195120 (2002).

[51] S. Bhattacharjee, E. Bousquet, and Ph. Ghosez, Phys. Rev. Lett. **102**, 117602 (2009).

[52] W. Luo, A. Franceschetti, M. Varela, J. Tao, S. J. Pennycook, and S. T. Pantelides, Phys. Rev. Lett. **99**, 036402 (2007).

[53] M. Nicastro, M. Kuzmin, and C. H. Patterson, Comput. Mater. Sci. **17**, 445 (2000).

[54] M. Nicastro and C. H. Patterson, Phys. Rev. B **65**, 205111 (2002).

[55] H. Meskine, H. König, and S. Satpathy, Phys. Rev. B **64**, 094433 (2001).

[56] J. H. Jung, K. H. Kim, D. J. Eom, T. W. Noh, E. J. Choi, Jaejun Yu, Y. S. Kwon, and Y. Chung, Phys. Rev. B **55**, 15489 (1997).

[57]G. Zampieri, F. Prado, A. Caneiro, J. Briático, M. T. Causa, M. Tovar, B. Alascio, M. Abbate, and E. Morikawa, Phys. Rev. B **58**, 3755 (1998).

[58]Z. Zeng, M. Greenblatt, and M. Croft, Phys. Rev. B **59**, 8784 (1999).

[59]J. Briático, B. Alascio, R. Allub, A. Butera, A. Caneiro, M. T. Causa, and M. Tovar, Phys. Rev. B **53**, 14020 (1996).

[60]G. S. Rushbrooke and P. J. Wood, Proc. R. Soc. London A **68**, 1161 (1955); Mol. Phys. **1**, 257 (1958).

[61]C. Toher and S. Sanvito, Phys. Rev. Lett. **99**, 056801 (2007).

[62]C. D. Pemmaraju, S. Sanvito, and K. Burke, Phys. Rev. B **77**, 121204(R) (2008).

[63]C. Toher and S. Sanvito, Phys. Rev. B **77**, 155402 (2008).

[64]I. Rungger, X. Chen, U. Schwingenschlögl, and S. Sanvito, Phys. Rev. B **81**, 235407 (2010).

[65]A. Droghetti and S. Sanvito, Phys. Rev. Lett. **107**, 047201 (2011).

[66]Larry A. Curtiss, Krishnan Raghavachari, Paul C. Redfern, and John A. Pople, J. Chem. Phys. **106**, 1063 (1997)

[67]N. Troullier and J. L. Martins, Phys. Rev. B **43**, 1993 (1991).

[68]C. Toher, A. Filippetti, S. Sanvito, and K. Burke, Phys. Rev. Lett. **95**, 146402 (2005).

[69]A. R. Rocha, V. M. Garcia-Suarez, S. Bailey, C. Lambert, J. Ferrer, and S. Sanvito, Phys. Rev. B **73**, 085414 (2006); Nat. Mater. **4**, 335 (2005).

[70]J. F. Janak, Phys. Rev. B **18**, 7165 (1978).

[71]J. P. Perdew, R. G. Parr, M. Levy, and J. L. Balduz Jr., Phys. Rev. Lett. **49**, 1691 (1982); J. P. Perdew and M. Levy, *ibid.* **51**, 1884 (1983).

[72]O. A. Vydrov and G. E. Scuseria, J. Chem. Phys. **122**, 184107 (2005).

[73]O. A. Vydrov, G. E. Scuseria, J. P. Perdew, A. Ruzsinszky, and G. I. Csonka, J. Chem. Phys. **124**, 094108 (2006).

[74]O. A. Vydrov and G. E. Scuseria, J. Chem. Phys. **124**, 191101 (2006).

[75]NIST Computational Chemistry Benchmark DataBase [http://srdata.nist.gov/cccbdb/default.html].

[76]T. Koopmans, Physica (Amsterdam) **1**, 104 (1933).

[77]L. Hedin and A. Johansson, J. Phys. B: At. Mol. Phys. **2**, 1336 (1969).

[78]A. Filippetti, Phys. Rev. A **57**, 914 (1998).

[79]V. I. Anisimov, F. Aryasetiawan, and A. I. Lichtenstein, J. Phys.: Condens. Matter **9**, 767 (1997).

[80]T. Zhu, J. Li, D. A. Liotard, C. J. Kramer, and D. G. Truhlar, J. Chem. Phys. **110**, 5503 (1999).

[81]P.-O. Löwdin, J. Chem. Phys. **18**, 365 (1950); B. C. Carlson and J. M. Keller, Phys. Rev. **105**, 102 (1957); I. Fischer-Hjalmars, in *Modern Quantum Chemistry (Istanbul Lectures)*, edited by O. Sinanöglu (Academic, New York, 1965); I. Mayer, Int. J. Quantum Chem. **90**, 63 (2002).